NASA/CR—2012-217664

Vibration Propagation of Gear Dynamics in a Gear-Bearing-Housing System Using Mathematical Modeling and Finite Element Analysis

Robert G. Parker, Yi Guo, Tugan Eritenel, and Tristan M. Ericson
The Ohio State University, Columbus, Ohio

August 2012

NASA STI Program . . . in Profile

Since its founding, NASA has been dedicated to the advancement of aeronautics and space science. The NASA Scientific and Technical Information (STI) program plays a key part in helping NASA maintain this important role.

The NASA STI Program operates under the auspices of the Agency Chief Information Officer. It collects, organizes, provides for archiving, and disseminates NASA's STI. The NASA STI program provides access to the NASA Aeronautics and Space Database and its public interface, the NASA Technical Reports Server, thus providing one of the largest collections of aeronautical and space science STI in the world. Results are published in both non-NASA channels and by NASA in the NASA STI Report Series, which includes the following report types:

- TECHNICAL PUBLICATION. Reports of completed research or a major significant phase of research that present the results of NASA programs and include extensive data or theoretical analysis. Includes compilations of significant scientific and technical data and information deemed to be of continuing reference value. NASA counterpart of peer-reviewed formal professional papers but has less stringent limitations on manuscript length and extent of graphic presentations.

- TECHNICAL MEMORANDUM. Scientific and technical findings that are preliminary or of specialized interest, e.g., quick release reports, working papers, and bibliographies that contain minimal annotation. Does not contain extensive analysis.

- CONTRACTOR REPORT. Scientific and technical findings by NASA-sponsored contractors and grantees.

- CONFERENCE PUBLICATION. Collected papers from scientific and technical conferences, symposia, seminars, or other meetings sponsored or cosponsored by NASA.

- SPECIAL PUBLICATION. Scientific, technical, or historical information from NASA programs, projects, and missions, often concerned with subjects having substantial public interest.

- TECHNICAL TRANSLATION. English-language translations of foreign scientific and technical material pertinent to NASA's mission.

Specialized services also include creating custom thesauri, building customized databases, organizing and publishing research results.

For more information about the NASA STI program, see the following:

- Access the NASA STI program home page at *http://www.sti.nasa.gov*

- E-mail your question to *help@sti.nasa.gov*

- Fax your question to the NASA STI Information Desk at 443–757–5803

- Phone the NASA STI Information Desk at 443–757–5802

- Write to:
  STI Information Desk
  NASA Center for AeroSpace Information
  7115 Standard Drive
  Hanover, MD 21076–1320

NASA/CR—2012-217664

Vibration Propagation of Gear Dynamics in a Gear-Bearing-Housing System Using Mathematical Modeling and Finite Element Analysis

Robert G. Parker, Yi Guo, Tugan Eritenel, and Tristan M. Ericson
The Ohio State University, Columbus, Ohio

Prepared under Contract NNC08CB03C

National Aeronautics and
Space Administration

Glenn Research Center
Cleveland, Ohio 44135

August 2012

This work was sponsored by the Fundamental Aeronautics Program at the NASA Glenn Research Center.

Level of Review: This material has been technically reviewed by NASA technical management OR expert reviewer(s).

Available from

NASA Center for Aerospace Information
7115 Standard Drive
Hanover, MD 21076–1320

National Technical Information Service
5301 Shawnee Road
Alexandria, VA 22312

Available electronically at http://www.sti.nasa.gov

Vibration Propagation of Gear Dynamics in a Gear-Bearing-Housing System Using Mathematical Modeling and Finite Element Analysis

Robert G. Parker, Yi Guo, Tugan Eritenel, and Tristan M. Ericson
The Ohio State University
Columbus, Ohio 43210

Contents

List of Figures

List of Tables

Abstract

Vibration and noise caused by gear dynamics at the meshing teeth propagate through power transmission components to the surrounding environment. The purpose of this work is to develop computational tools to investigate the vibro-acoustic propagation of gear vibration and to investigate the effect of different bearing types on noise radiation. Detailed finite element/contact mechanics and boundary element models of the gear/bearing/housing system are established to compute the system vibration and noise propagation. Both vibration and acoustic models are validated by experiments including vibration modal testing and sound field measurements.

Bearings are critical components in drivetrains. Accurate modeling of rolling element bearings is essential to assess vibration and noise of drivetrain systems. This study also seeks to fully describe the vibro-acoustic propagation of gear dynamics through a power-transmission system using rolling element and fluid film wave bearings. Fluid film wave bearings have higher damping than rolling element bearings and so could offer an energy dissipation mechanism that reduces the gearbox noise. The effectiveness of each bearing type to disrupt vibration propagation is explored using multi-body computational models. These models take into account gears, shafts, rolling element and fluid film wave bearings, and the housing. Radiated noise is mapped from the gearbox surface to surrounding environment. The effectiveness of each bearing type to disrupt vibration propagation is speed-dependent. Housing plays an important role in noise radiation. It, however, has limited effects on gear dynamics.

1 Introduction

Gearbox vibration contributes the structural-borne noise in helicopters [9]. The gearbox noise consists of a wide range of gear mesh, shaft, and bearing frequencies within relative lower audio frequency range than the jet engine noise, which is another source of helicopter structural-borne noise. Systematic studies of the noise and vibration behavior are essential to design quiet helicopters and to identify noise and vibration sources. Limited work has, however, investigated the relationship between the gearbox noise and vibration.

Experimental vibro-acoustic analysis of helicopters requires effort [9, 10, 11, 12, 13] because advanced signal processing techniques are needed to separate the gear, shaft, and bearing signals [14]. The analytical or computational vibro-acoustic analysis of geared systems is also sparse [15] in the literature due to the complexity of these problems. Structural-borne noise calculations of geared systems are, furthermore, semi-empirical [16, 17]. These

acoustic models are not able to capture realistic dimensions of gearboxes which often have complicated structures, which affect the noise estimate. This work defines the vibro-acoustic behavior of gear dynamics through power-transmission systems using multi-body dynamics gearbox models established in [18, 19] and an in-house program.

Dynamic forces at the meshing teeth drive a system vibration through power transmission components to the fuselage. The bearings linking the gear shafts to the housing are a primary factor in this noise path. Fluid film wave bearings are a special type of journal bearings, which have waved inner diameters of the stationary bearing sides shown in Figure 1. The wave profile amplitude is a few micrometer so that it is not obvious in this figure. The wave bearing technology used for gas turbine lubrication [20, 21] is recently applied to the planet bearings used in aviation planetary gears [22, 23, 20]. This technology provides higher stiffness and better lubrication for the bearings. Experiments on an aviation gearbox [22] with wave bearings demonstrate 25% higher load capacity compared to plain journal bearings. Dimofte [20] compared the load capacity between wave and journal bearings through an analytical formulation. He concluded that wave bearings are more stable than plain journal bearings under light-load or unloaded conditions in any operating regime. Furthermore, wave amplitude and starting positions of the wave profiles are important parameters affecting wave bearing performance.

Machinery applications use rolling element bearings that do not create meaningful damping to reduce the transmitted structural-borne noise. Wave bearings have higher damping [24] and could offer energy dissipation. If fluid film wave bearings are shown to withstand harsh operating conditions and provide better vibration characteristics, they may prove an attractive alternative to standard rolling element bearings.

The major objectives of this study are to: 1) develop a finite element gearbox model which includes the detailed contact analysis of the gear tooth mesh and individual bearing rolling elements; 2) build up analytical (lumped parameter) model of the gear/bearing/housing system, which provides efficient dynamic analysis; 3) establish a boundary element model of the gearbox housing and map the radiated noise from the gearbox surface through acoustic analysis; 4) validate the vibration and acoustic models of the examined gearbox against measurements and theoretical solutions in the literature; and 5) understand the effectiveness of fluid film wave bearings in breaking the vibro-acoustic propagation path from the gears to the housing.

Figure 1: Fluid film wave bearing.

2 Preliminary Step: Experimental Modal Test

Frequency response measurements provide vital system information: natural frequencies, mode shapes, and damping characteristics. Modal analysis by impact testing establishes a baseline of comparison for mathematical simulations. Computational and analytical tools are used to fully characterize the performance of rolling element and fluid film wave bearings. Experimental measurements provide benchmarks, against which mathematical models are validated.

Impulse test data was collected on the NASA GRC gear test rig by Ohio State researchers in November, 2008. Data was collected to provide frequency response curves of the gear test rig for multiple inputs and outputs. This data provides transfer functions across system components and can be used to extract vibration mode shapes. A standard impact hammer with built-in force transducer was used to provide a known input excitation. Accelerometers were used to obtain dynamic response. The known input and measured output yield system frequency response characteristics that are independent of the testing method. These results help predict the system behavior in response to gear vibration, establishing benchmarks that validate the modeling effort. The experimental study also helps defining the system for computational/analytical study.

At the time of the OSU experiments, four accelerometers were already installed by NASA researchers. One accelerometer was mounted vertically and one horizontally on each of the pinion shaft bearings. Nine additional accelerometers were mounted and used by OSU to measure the frequency response around the test gearbox. Figure 2 shows the approximate locations of these accelerometers mounted in and around the gearbox. Impact tests were performed throughout the system. This report contains findings from four of the most relevant impact tests. Figure 3 identifies the impact locations for these four tests. Three impacts were averaged for each experiment. Data was taken with the gearbox cover

off to measure vibrations inside the gearbox. The subsequent results are shown on a dB scale.

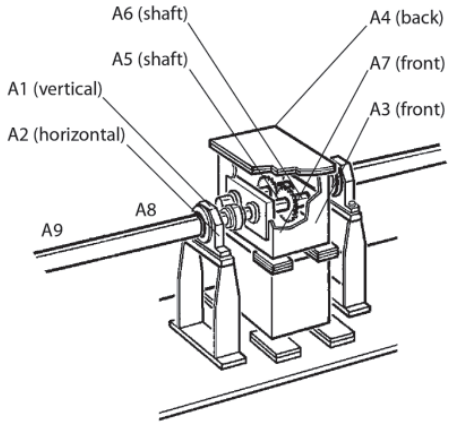

Figure 2: Nine mounting locations for additional OSU accelerometers in and around gearbox.

2.1 Translational Impact to Gear Tooth

In this test an impact was made to a gear tooth to simulate excitation near the meshing gears. Figure 3(a) shows the impact point and two relevant accelerometers mounted on the pinion shaft (A5 and A6). The averaged frequency response function from the NASA accelerometers is shown in Figure 4(a). The frequency response functions from the relevant OSU accelerometers for this test are shown in Figure 4(b).

The data in Figure 4 shows distinct natural frequencies at $750\,Hz$ and $2500\,Hz$ in the NASA bearing accelerometers (a) and the additional accelerometers (A5 and A6) mounted to the pinion shaft (b). The pinion shaft also shows a smaller peak around $1800\,Hz$. Both graphs show less-defined dynamic behavior between 3300 Hz and $3800\,Hz$. Accelerometers A1 and A2, which are mounted to the input shaft pillow block outside the gearbox (Figure 2), show a reduction of vibration amplitudes by about 20 dB. This shows that vibration propagation is well-contained within the gearbox. Most importantly, this test shows two natural frequencies associated with the gears and/or shafts at $750\,Hz$ and $2500\,Hz$ which appear to be contained within the gearbox.

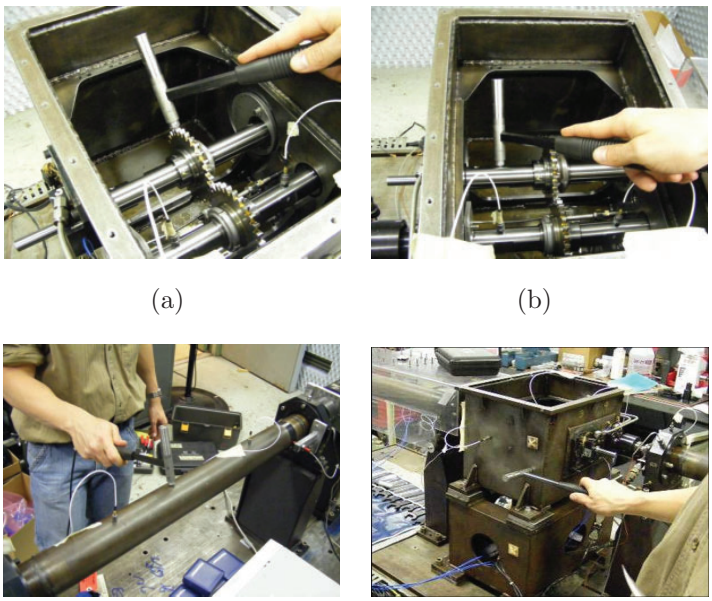

(a) (b)

(c) (d)

Figure 3: Impact locations for relevant tests: (a) translational impact to gear tooth with accelerometers A5 and A6 mounted to the pinion shaft, (b) impact to output gear shaft with accelerometers A5 and A6 mounted to the pinion shaft, (c) impact to rig input shaft with accelerometers A8 and A9 mounted to the input shaft, (d) impact to rear of gearbox housing with accelerometers A3, A4 and A7 mounted to the gearbox housing.

2.2 Translational Impact to Gear Shaft

In this test an impact was made to the output gear shaft, between the gear and the supporting bearings. This impact location is near the previous test, and it was performed to determine if the dominant $750\,Hz$ and $2500\,Hz$ peaks are predominantly gear or shaft modes. Figure 3(b) shows the impact point and two relevant accelerometers mounted on the pinion shaft (A5 and A6). The averaged frequency response function from the NASA accelerometers and the frequency response functions from the relevant OSU accelerometers for this test are shown in Figure 5(b) and compared to the results from the previous test to the gear tooth in Figure 5(a).

The results from the test on the gear shaft show the same two dominant peaks at $750\,Hz$ and $2500\,Hz$. The amplitudes, however, have changed significantly. The $750\,Hz$ peak is about 5 dB higher in the impact to the gear tooth, but the $2500\,Hz$ peak is about 10 dB higher in the impact to the gear shaft. This suggests that the $2500\,Hz$ mode is

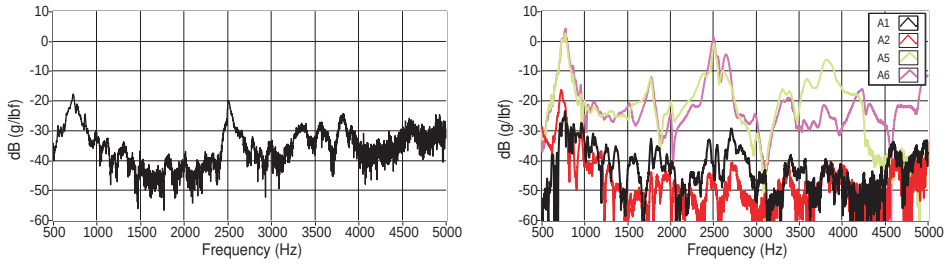

(a) (b)

Figure 4: Frequency response functions for impact test to output gear tooth with accelerometers A5 and A6 mounted to the pinion shaft and accelerometers A1 and A2 mounted to the input shaft pillow block for (a) mean NASA accelerometers and (b) select OSU accelerometers.

dominated by shaft vibration and the 750 Hz mode has more gear body translation.

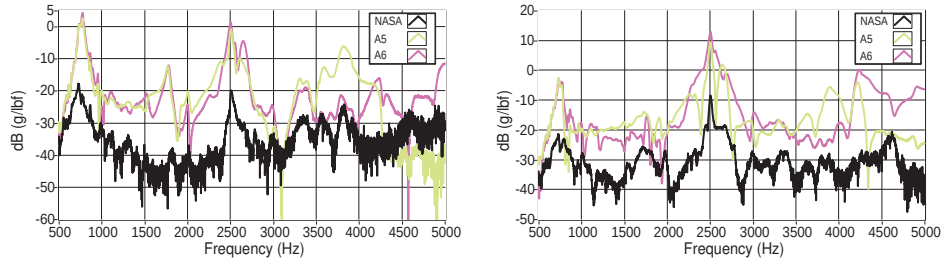

(a) (b)

Figure 5: Frequency response comparison for (a) impact to pinion gear tooth, and (b) impact to gear shaft.

2.3 Impact to Gearbox Input Shaft

In this test an impact was made to the large, hollow input shaft of the test rig. This test was performed to measure vibration transmissibility into and out of the gearbox. Knowing that this shaft (and the output shaft like it) will have bending and torsional modes within the frequency range of interest, it was necessary to determine if these accessory components were coupled to the gearbox system under study. Figure 3(c) shows the impact point and two relevant accelerometers mounted on the input shaft itself (A8 and A9). All four frequency response functions from the NASA accelerometers are shown in Figure 6(a). The frequency response functions from the relevant OSU accelerometers for this test are shown in Figure 6(b).

The data in Figure 6(b) shows five distinct natural frequencies of the input shaft between 3050 Hz and 4500 Hz, measured by A8 and A9. This is within the frequency range of expected gear dynamics. Therefore, if the input shaft is coupled with the gearbox system, it would need to be modeled. Accelerometers A1 and A2, which are mounted to the input shaft pillow block outside the gearbox (Figure 2), show a reduction of vibration amplitudes by at least 20 dB and do not pick up any of the input shaft modes. In addition, all four NASA bearing accelerometers do not pick up any vibration from this impact, not even in trace vibrations between 3050 Hz and 4500 Hz. This suggests that the gearbox system under study is not coupled with the accessory drive components and permits confident modeling of the chosen system.

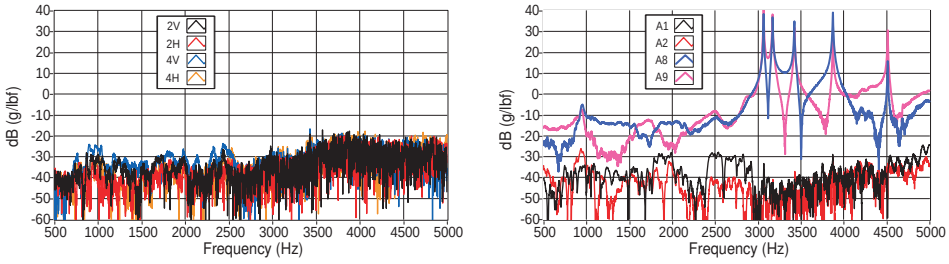

(a) (b)

Figure 6: Frequency response functions for impact test to gearbox input shaft with accelerometers A8 and A9 mounted to the input shaft and accelerometers A1 and A2 mounted to the input shaft pillow block for (a) four NASA accelerometers and (b) select OSU accelerometers.

2.4 Impact to Rear of Gearbox Housing

In this test an impact was made to the rear of the gearbox housing to estimate the dominant gearbox structural modes. Figure 3(d) shows the impact point and one of the accelerometers mounted to the gearbox (A4). The mean frequency response function from the NASA accelerometers is shown in Figure 7(a), and the frequency response functions from the relevant OSU accelerometers for this test are shown in Figure 7(b).

Figure 7(b) shows multiple natural frequencies picked up by accelerometers mounted to the gearbox housing: 550 Hz, 1000 Hz, 2000 Hz, and 2800 Hz. Two of these peaks (2000 Hz and 2800 Hz), are evident in the NASA bearing accelerometers of Figure 7(a), but the two lower-frequency peaks are not apparent. This data provides an estimate of the primary gearbox modes and shows which of these includes significant bearing dynamics.

As seen before, accelerometers A1 and A2, which are mounted to the input shaft pillow block outside the gearbox, show a reduction of vibration amplitudes by about 20 dB and hardly pick up the natural frequencies at 2000 Hz and 2800 Hz. This adds confidence to the assumption that the gearbox system under study is not significantly coupled with the accessory drive components, validating the modeling approach.

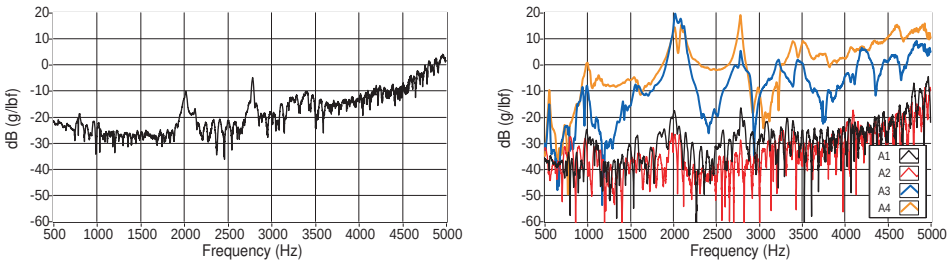

(a) (b)

Figure 7: Frequency response functions for impact test to rear of gearbox housing with accelerometers A3 and A4 mounted to the front and rear of gearbox respectively and accelerometers A1 and A2 mounted to the input shaft pillow block for (a) mean NASA accelerometers and (b) select OSU accelerometers.

2.5 Impact Test Summary

Important information was learned from these brief impulse tests. General system behavior was characterized by identifying several important natural frequencies. With thirteen total accelerometers, it was easy to identify the components of principal vibration at these natural frequencies. These tests also helped establish boundaries of the system for computational and analytical studies. While the gears, shafts, bearings, and housing are clearly coupled, it is apparent that connecting input/output shafts, pillow blocks, the drive motor, and dynamometer structure do not contribute significantly to the dynamic behavior of the system. Table 1 summarizes the modes identified in this study and the most significant components of vibration.

Table 1: Natural frequencies observed in the NASA GRC gear test rig by impact testing.

Number	Frequency	Primary component
1	$500\,Hz$	Gearbox
2	$750\,Hz$	Gears/shafts
3	$1000\,Hz$	Gearbox
4	$1800\,Hz$	Shafts
5	$2000\,Hz$	Gearbox/bearings
6	$2500\,Hz$	Gears/shafts
7	$2800\,Hz$	Gearbox/bearings
8-12	$3050\,Hz - 4500\,Hz$	Input shaft (accessory)

3 Gearbox Vibro-Acoustic Propagation Analysis Method Overview

The vibro-acoustic gearbox modeling consists of four parts. They are: 1) full-fidelity finite element/contact mechanics model of the entire gearbox including gears, shafts, bearings, and the housing [18]; 2) mathematical lumped-parameter gearbox model; 3) finite element housing model; and 4) boundary element model of the housing [19].

The finite element model of the analyzed gearbox (shown in Figures 8(a) and 8(b)) includes realistic rolling element bearings, shafts, and the housing. Other models may model these components analytically because of the modeling complexity. The unique contact algorithm seeks the gear and rolling element contact in three-dimensional space. This algorithm has been validated against experiments [25, 26, 27, 28, 29, 30, 31]. Output of this detailed finite element model includes dynamic bearing force, bearing stiffness, and transmission error, which are crucial information for the acoustic analysis and mathematical modeling.

The analytical model of the gearbox provides fast dynamic analysis of the gearbox. Bearings are modeled as linear stiffnesses using 6×6 matrices computed by the finite element/contact analysis. Housing is included through its static condensation compliance matrix, computed by finite element analysis. The gear contact is modeled by a network of springs along lines of contact. The gear model is nonlinear and captures the non-nominal load distributions due to shaft tilting, misalignment, and profile/lead modification.

Isolated finite element housing model is established in ANSYS. The housing excitation source is dynamic bearing forces calculated using the finite element/contact or analytical model. The surface velocity of the bearing is obtained by the dynamic responses. This step can not be omitted because it connects the vibration analysis of the entire gearbox and the housing noise radiation computation in the following step.

The full-fidelity boundary element model of the gearbox housing is established in the software Coustyx [32, 19]. The acoustic model employees a multipole method ([32]) to provide noise calculation with realistic housing dimensions. This housing surface velocity calculated by ANSYS is inputted into the acoustic model as its boundary condition. This acoustic model computes the radiated noise from the housing.

Major steps of the gearbox vibro-acoustic analysis is depicted in Figure 9.

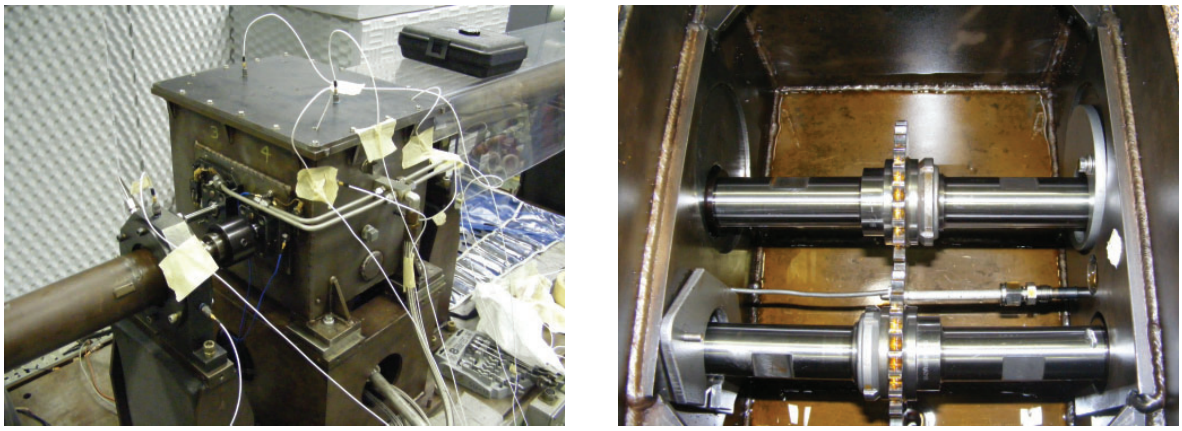

(a) (b)

Figure 8: (a) Outside and (b) inside of the gearbox at NASA Glenn Research Center.

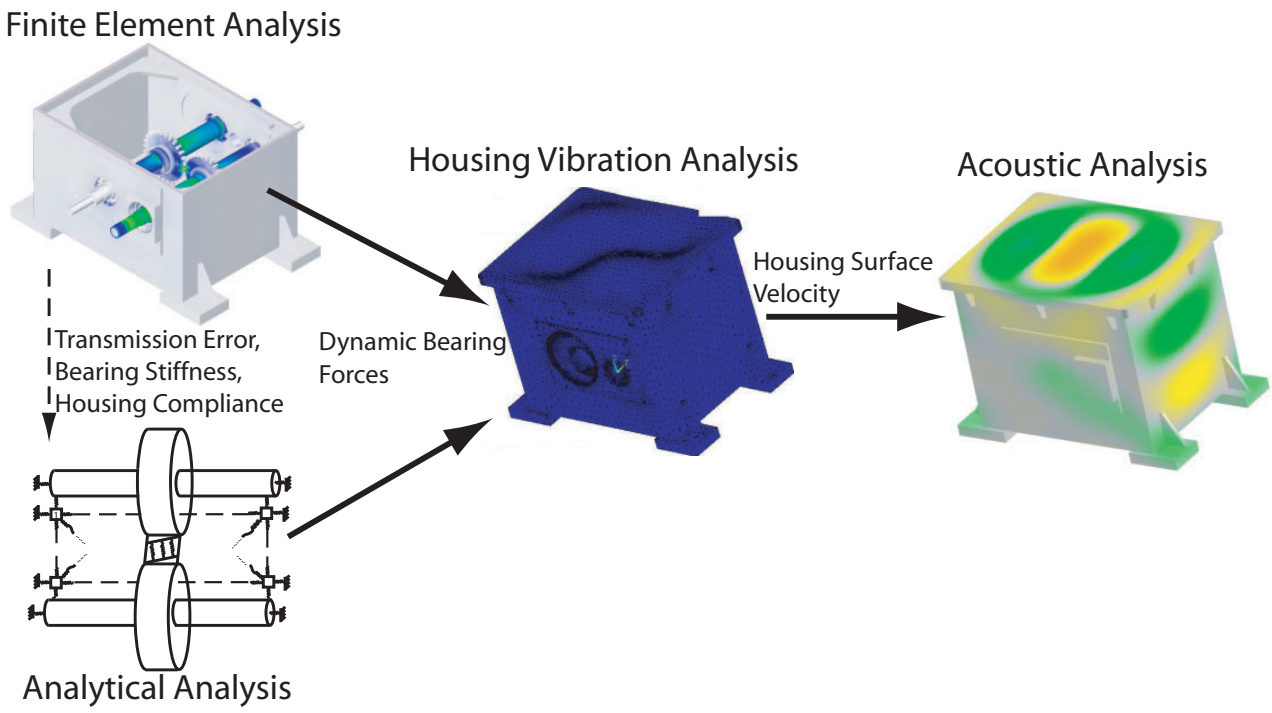

Figure 9: Key steps to perform the gearbox acoustic analysis.

4 Finite Element/Contact Mechanics Modeling and Analysis of the Gearbox

4.1 Gearbox Modeling Overview

The examined NASA GRC gearbox (shown in Figures 8(a) and 8(b)) includes a pair of spur gears with webbed rims, two staged shafts on which the gears are mounted, four rolling element bearings that support the shafts, and the housing. The gear parameters are listed in Table 3. Two types of rolling element bearings are used: cylindrical rolling bearings and deep groove ball bearings (described in Table 2). Product designations are SKF N205ECP and SKF 6205, respectively. The height and width of the gearbox housing is 279.4mm and 254.0mm with 330.2mm length. The housing wall and lid thickness is 6.350mm. Details of the gearbox are described in [33, 24].

The realistic bearing model captures detailed bearing mechanics as shown in Figure 10, including rolling elements, races, and the cage (not shown). This detailed bearing model is used to determine the full 6×6 stiffness matrix between the shafts and housing. That matrix is used in the mathematical gearbox model to perform fast dynamic simulations,

Parameters (mm,degree)	*Cylindrical Roller*	*Ball Bearing*
Number of rows	1	1
Number of rolling elements	13	9
Contact angle	0	0
Pitch diameter	39.00	38.50
Bore diameter	25.00	25.00
Roller length	8.600	7.900
Roller diameter	7.500	7.900
Bearing width	15.00	15.00
Outer diameter	52.00	52.00
Outer diameter of inner raceway	31.50	34.40
Inner diameter of outer raceway	46.40	46.30
Radial clearance	40.00×10^{-3}	20.00×10^{-3}
Inner race crown curvature	10^{-7}	0.520
Outer race crown curvature	10^{-7}	0.520

Table 2: Single row cylindrical roller and ball bearing parameters.

as discussed later.

The gearbox housing is modeled by importing the full fidelity mesh established in commercial finite element software, PATRAN. The housing is then assembled into the gear/bearing/shaft system as shown in Figure 11.

4.1.1 Contact Solver

The contact solver of [18] seeks contact between gear teeth and bearing rolling elements and raceways. Mesh stiffness variation, transmission error, tooth separation, and bearing stiffness variation are inherently included; they are outputs rather than inputs. Transmission error is the major excitation source in geared systems [34] so an accurate transmission error estimate is crucial. The finite element/contact analysis of the gearbox provides the required reliable transmission error estimate.

The geometric surface descriptions of the contacting bodies must be precise to fully address the contact characteristics. Additionally, the contact area is narrow and travels over the entire body surface. Conventional finite element analysis requires a prohibitively

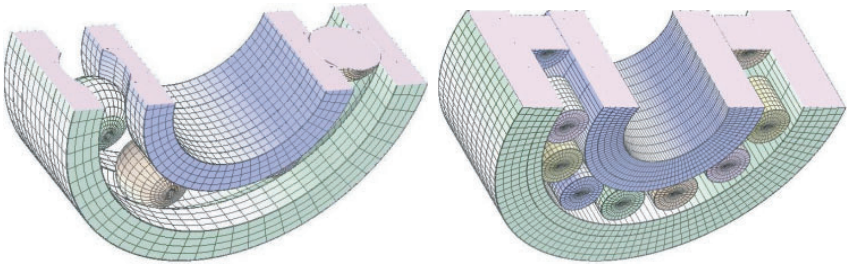

(a) (b)

Figure 10: Cut-away finite element mesh of the radial ball bearing used in the gearbox (dimensions detailed in Table 2) and a double-row cylindrical rolling element bearing (from a helicopter application).

Parameters	*Values (mm, degree)*
Number of teeth	28
Outer diameter	95.25
Root diameter	79.73
Facewidth	6.350
Module	3.175
Pressure angle	20
Center distance	88.90
Tooth thickness	4.851
Cutter edge radius	1.270
Linear tip relief	0.1778 starting at 24 degrees

Table 3: Dimensions of the spur gear pair

refined mesh to address these problems; a complete dynamic response analysis becomes impossible in that case.

The finite element/contact mechanics model used here addresses these issues by using a combination of the Boussinesq solution near the contacting surfaces and traditional finite element analysis far away from the contact zones to exploit the advantages of each. The details about this contact solver can be found in [35].

To accurately describe the contact area and pressure, the contact zone is discretized into many small patches (grid cells). Sufficient number of grid cells within the contact

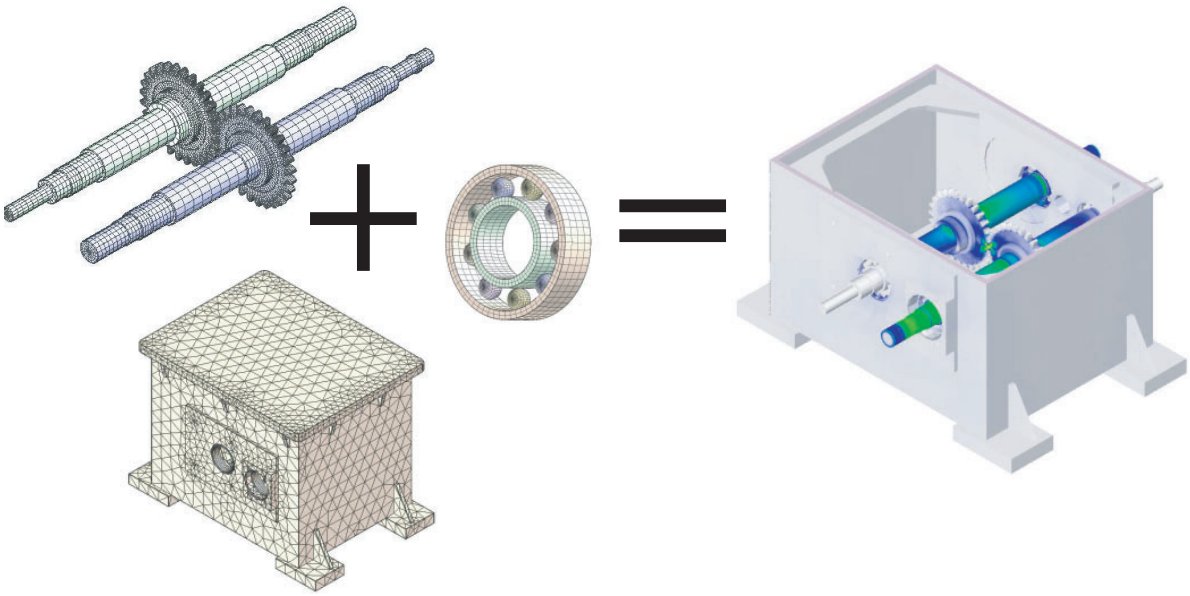

Figure 11: Assembly of the gear-bearing-shaft-housing model.

zone is essential to obtain the correct contact pressure and load distribution. The finite element model of the gear pair and contact pressure on individual tooth over a mesh cycle are shown in Figure 12(a) and Figure 12(b). Figure 13(a) shows the finite element model of a double-row cylindrical rolling element bearing. Contact patches on one of the radially loaded cylinders are shown in Figure 13(b).

When the gears and rolling elements rotate, the number of teeth and rolling elements in contact change, as do the location, size, and shape of the contact areas. These changes are important as they affect bearing forces, gear tooth loads, and transmission error calculations. The contact solver addresses these issues by determining and analyzing the instantaneous gear and bearing contact conditions at every time instant.

This specialized finite element/contact mechanics software allows dynamic simulations with greater modeling fidelity than conventional finite element tools. It is validated against benchmark studies of complex gear dynamics problems [25, 26, 27, 28, 29, 30]. In experimental comparisons, it has proven accurate in capturing the complex tooth mesh forces leading to strong nonlinearity in the dynamics of single gear pairs [26], idler [29, 36], and planetary gears [25, 27, 28, 37]. The rolling element contact in multiple bearings has been validated against experiments in [31]. The shafts in the gearbox introduce system compliance, could cause misalignment, and eventually affect transmission error. The accuracy of the shaft models have been validated against classical beam theories as discussed later.

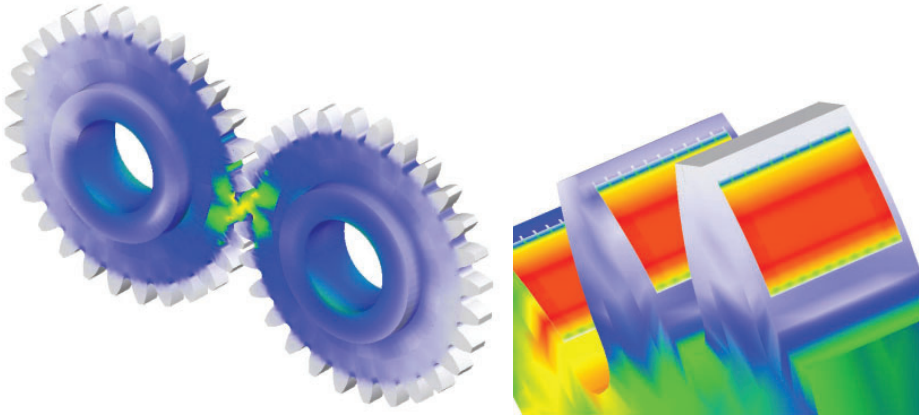

(a) (b)

Figure 12: (a) Mating gears in the NASA GRC gearbox; (b) contact pressure on gear teeth over one mesh cycle;

4.2 Fluid Film Wave Bearing Modeling

Bearings are critical components in geared systems. The fluid film wave bearings are included in the gearbox model through the stiffness and damping matrices calculated by the program developed by Hanford and Campbell [38, 39]. This wave bearing model uses a perturbation method based on the Reynold equation to calculate the stiffness, damping, pressure distribution, and load capacity of the fluid film. The program, however, is limited to be two-dimensional by excluding the bearing tilting motion.

4.3 Rolling Element Bearing Modeling and Analysis

Theoretical bearing models [1, 40, 41, 42] make different assumptions to formulate the load-deflection relation. These assumptions include different race elasticity, different property of the rolling element contact, and ignoring microgeometry dimensions of bearing raceways. Figure 14 shows the nonlinear stiffness-load relations of the cylindrical and radial ball bearings calculated using the Harris [1], Gargiulo [2], and While [3] models. Significant discrepancy is present among them.

The method developed to determine bearing stiffness does not make any assumptions about the load-deflection relation. Instead, it calculates the 6×6 bearing stiffness matrix by partial derivatives of applied forces and moments related to six degrees of freedom. This

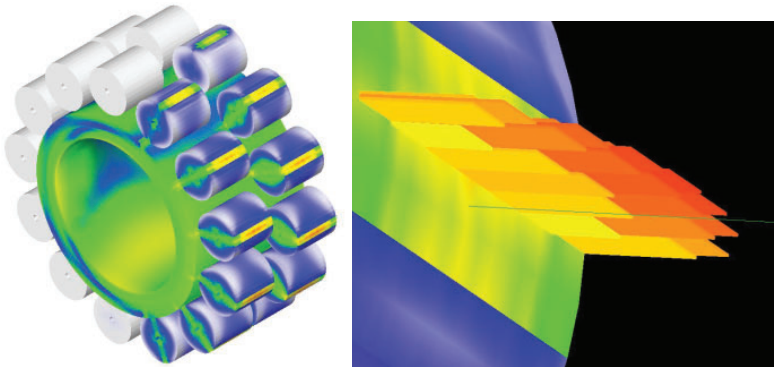

(a) (b)

Figure 13: (a) Finite element model of a double row cylindrical bearing (outer race is removed); (b) contact pattern on one of the loaded cylinders.

stiffness determination approach is detailed in [31].

Radial and axial stiffness of radial ball bearing in [4] calculated by the proposed method under axial preloads is compared against the experiment conducted by Kraus et. al. in [4] as shown in Figure 15. Because of the lack of information on internal radial clearance, two clearance values of 0 and 0.01 mm are used to compute stiffness. Radial and axial stiffness of self-aligning ball bearing in [5] calculated by the proposed method is compared against the Royston and Basdogan [5] experiment under radial and axial preloads, respectively (Figure 16). Good agreement is evident between the proposed method and the measurements for both bearings.

The number of rolling elements in contact oscillates when they rotate, which indicates bearing stiffness is periodic about the ball pass frequency. The ball pass period $T = \frac{2}{Z\omega(1-\frac{D_e}{D_p})}$ is the amount of time between one rolling element leaving a reference point and the next rolling element arriving. Here, z is the number of rolling elements, ω denotes the shaft speed, and quantities D_e and D_p denote the diameter of rolling elements and pitch diameter of the bearing, respectively.

Figures 17(a) and 18(a) show radial stiffness of the cylindrical and radial ball bearings in a ball pass period with 1000 N applied load. Radial stiffness of the cylindrical bearing fluctuates with 16% deviation from the mean stiffness, while the number of rolling elements in contact alternates between four and five over the ball pass period. Figures 17(b) and 18(b) show tilting stiffness of the cylindrical and ball bearings when 1 Nm moment is applied. These stiffness fluctuations can excite gearbox vibration.

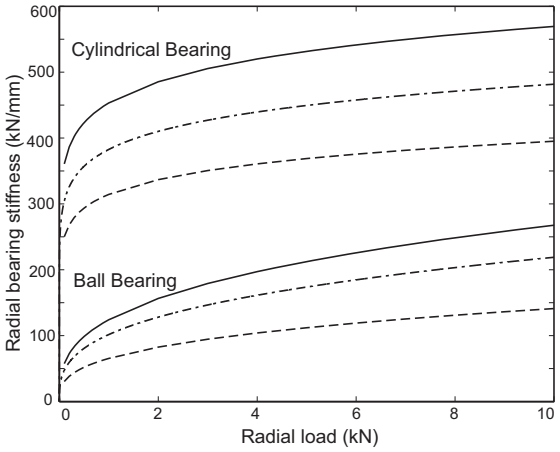

Figure 14: Radial stiffness of examined cylindrical bearing and radial ball bearing vs. applied radial loads calculated by the Harris (−) [1], Gargiulo (· − ·−) [2], and While (−−) [3] models. The While [3] model is modified to use $\frac{\Delta F}{\Delta q}$ to calculate the stiffness instead of $\frac{F}{q}$.

4.3.1 Cross-Coupling Bearing Stiffnesses

Traditionally, diagonal stiffness matrices are used to represent rolling element bearings. These stiffness matrices, however, include both diagonal and off-diagonal terms. Equation 1 demonstrates the stiffness matrix structure. The quantities k_{xx}, k_{yy} denote radial stiffness. k_{zz} denotes axial stiffness. The quantities $k_{\theta_x\theta_x}$, $k_{\theta_y\theta_y}$ denote tilting stiffness, which prevents the tilting motion of the shafts. The off-diagonal stiffness falls into four categories: the coupling between radial and rotational displacements ($k_{x\theta_x}$, $k_{x\theta_y}$, $k_{y\theta_x}$, $k_{y\theta_y}$), the coupling between radial and axial displacements (k_{xz}, k_{yz}), the coupling between axial and rotational displacements ($k_{z\theta_x}$, $k_{z\theta_y}$), and other coupling terms (k_{xy}, $k_{\theta_x\theta_y}$). Rolling elements are free to rotate in θ_z direction so that stiffness in θ_z direction and other related matrix components are zeros. The stiffness matrix is symmetric because rolling element bearings are conservative systems.

$$\mathbf{K} = \begin{bmatrix} k_{xx} & k_{xy} & k_{xz} & k_{x\theta_x} & k_{x\theta_y} & 0 \\ & k_{yy} & k_{yz} & k_{y\theta_x} & k_{y\theta_y} & 0 \\ & & k_{zz} & k_{z\theta_x} & k_{z\theta_y} & 0 \\ & & & k_{\theta_x\theta_x} & k_{\theta_x\theta_y} & 0 \\ & Symmetric & & & k_{\theta_y\theta_y} & 0 \\ & & & & & 0 \end{bmatrix} \tag{1}$$

Cross-coupling terms in the stiffness matrix indicate interactions between radial, axial,

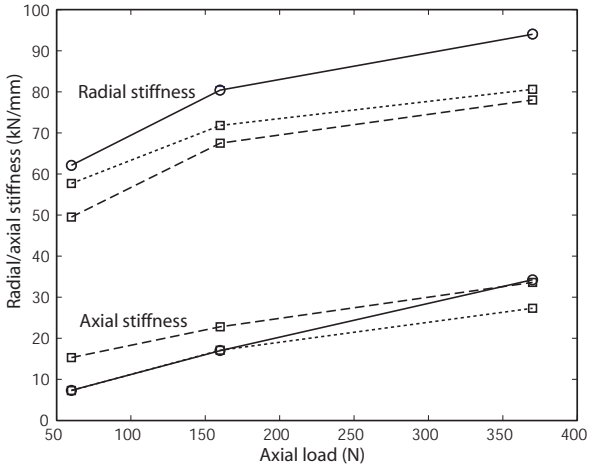

Figure 15: Comparison between the proposed method with zero ($\cdots\square\cdots$) and 0.01 mm ($\cdot - \square \cdot -$) radial clearances and Kraus et al.'s [4] experiment ($- \circ -$) for radial and axial stiffness of the ball bearing in [4] under axial preloads.

and tilting motions of rolling element bearings. They demonstrate the coupling between the shaft tilting motion, the flexural motion of the structure connected to the outer race, and the shaft radial and axial motions. The effects of cross-coupling terms on the gearbox vibration transmissibility through rolling element bearings are investigated. As the primary excitation source, gear transmission error is an important measure of gearbox vibration. Figure 19 shows the spectra of dynamic transmission error in the frequency range from 1500 to 4000 Hz from numerical torque impulse cases. Bearing models with fully-populated and diagonal stiffness matrices are compared as shown in Figure 19. Differences in resonant frequencies and amplitudes are evident between these two bearing models. This stresses the significance of the cross-coupling stiffnesses.

4.4 Gear Transmission Error

Transmission error is the major excitation source in geared systems. Accurate transmission error estimate is crucial. With the precise contact solver, the finite element/contact analysis of the gearbox provides reliable transmission error estimate.

Transmission error is computed according to the tooth mesh deflection $TE = (x_1 - x_2)sin(\alpha) + (y_1 - y_2)cos(\alpha) + r_1\theta_1 + r_2\theta_2$, where x_i, y_i, θ_i, $i = 1, 2$ are the coordinates of the mating gears as shown in Figure 20. α is the pressure angle and r_i, $i = 1, 2$ are the radii of the meshing gears. This formulation includes the shaft and bearing compliance.

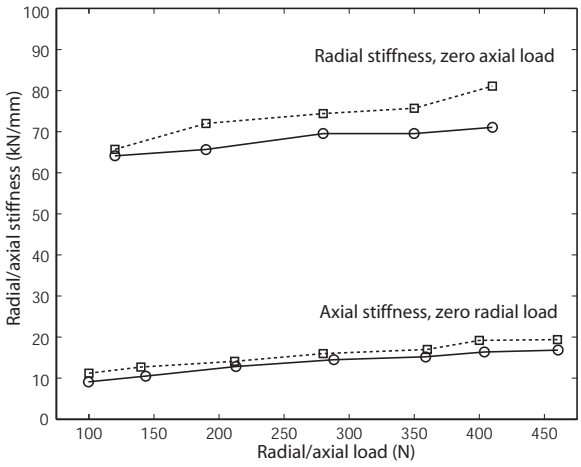

Figure 16: Comparison between the proposed method ($\cdots\square\cdots$) and Royston and Basdogan [5] experiment ($-\circ-$) for radial and axial stiffness of self-aligning ball bearing in [5] under radial and axial preloads, respectively.

Transmission error of this gear pair without shaft or bearing compliance has been compared among Program X, Load Distribution Program, NASA DANST [43], and the current approach in Figure 21. Program X is multi-body dynamics software that is used by industries worldwide. We are not free to state its name because of license restrictions for academic use. The agreement on the peak to peak amplitude is reasonable. Differences among the mean amplitudes are present. These differences are mainly caused by different rim models these programs have used. Gear rims introduce compliance into the system, leading to high amplitude of the mean transmission error. The current model includes the realistic rim (as shown in Figure 12(a)). Others model the rims differently by excluding the rim shoulders. Thus, their estimates of transmission error are lower. The Harris map of transmission error at various torques is shown in Figure 22. The minimum transmission error without including the shaft compliance is at $67.79\,Nm$ torque, which matches the torque the gear teeth are modified at. This further validates the transmission error estimate.

In addition, the minimum of the peak to peak value of transmission error is at lower torque ($57.62\,Nm$) when flexible shafts are included as shown in Figure 22. This suggests shaft compliance needs to be considered to estimate transmission error and modify gear

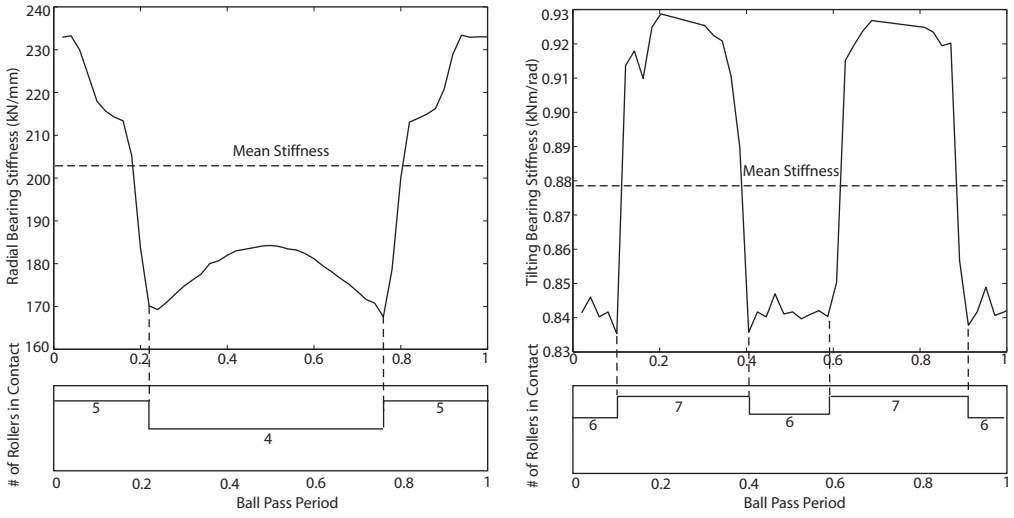

(a) (b)

Figure 17: (a) Radial and (b) tilting stiffness of the cylindrical bearing over a ball pass period. The bottom figures show the number of rolling elements in contact over a ball pass period. The applied load and moment are $1000\,N$ and $1\,Nm$, respectively.

teeth.

4.5 Shaft Modeling and Validation

The long shafts in the gearbox introduce system compliance, could cause misalignment, and eventually affect transmission error. The accuracy of the shaft models are important.

The shaft bending and torsional deformations are compared against classical beam theories. The shaft bending model is considered as the elastic beam with a concentrated load applied at the gear location. The beam bending boundary conditions are chosen as simply-supported at each end of the shaft. The transverse deflection y along the shaft is calculated as

$$y = \frac{Pb[x^3 - \left(L^2 - b^2\right)x]^{3/2}}{6EIL}, x < a$$
$$I = \frac{\pi\left(R_{out}^4 - R_{in}^4\right)}{4} \tag{2}$$

where the parameter P is the applied concentrated force. The parameters a, b are the distances between one shaft end and the location where P is applied. The quantities E, I, L denote the Young's modulus, moment of inertia, and shaft length. The quantities R_{out}, R_{in} denote the shaft outer and inner radii.

The analytical model to calculate the shaft torsional deflection has the clamped-free

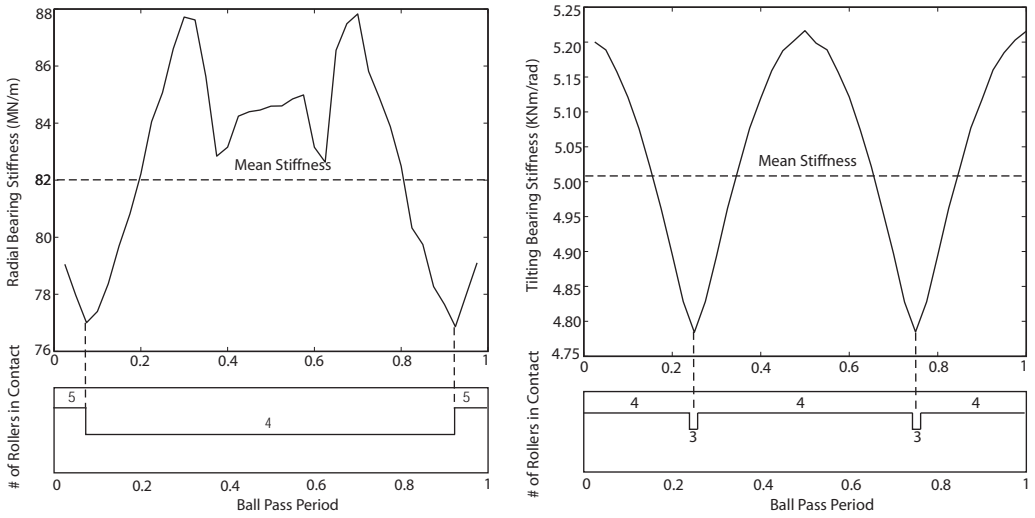

(a) (b)

Figure 18: (a) Radial and (b) tilting stiffness of the ball bearing over a ball pass period. The bottom figures show the number of rolling elements in contact over a ball pass period. The applied load and moment are $1000\,N$ and $1\,Nm$, respectively.

boundary condition. A torque T is applied at the free end of the shaft. The torsional deflection θ is calculated as

$$\theta = Tx/GJ$$

$$G = \frac{E}{2(1+\nu)} \tag{3}$$

$$J = \frac{\pi}{2}\left(R_{out}^4 - R_{in}^4\right)$$

where the quantities ν, J denote the Possion's ratio and the second moment of inertia.

Figures 23(a) and 23(b) show the shaft bending and torsional deformations calculated by analytical solutions (solid line) and finite element results (square marker) at various torques/forces. The finite element results of shaft bending and torsional deformations agree with the analytical predictions.

In addition, as shown in Figure 4.5, the bending deformation is the same order of magnitude of transmission error near the operating torque. Shaft deformation is significant. Thus, including shafts would increase the overall accuracy of gearbox modeling.

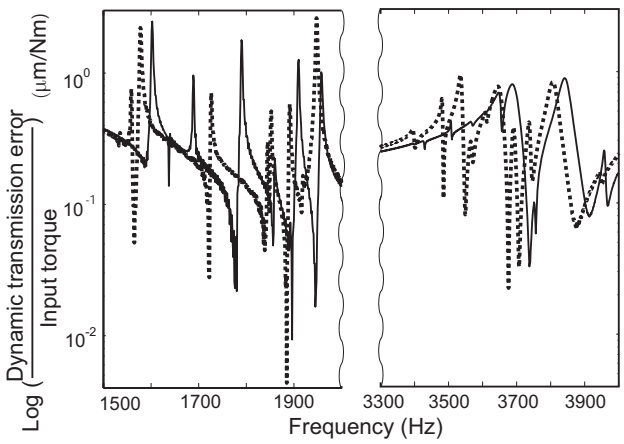

Figure 19: Numerical torque impulse response of gear dynamic transmission error with fully-populated ($-$) and diagonal ($--$) stiffness matrices of the rolling element bearings mounted in the examined gearbox based on [6]. The input torque equals $84.74\,Nm$.

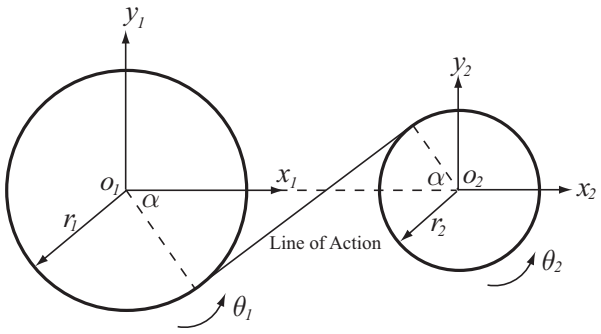

Figure 20: Coordinates of the examined gear pair.

4.6 Dynamic Analysis and Correlation with Experiments

Modal analysis is performed numerically on the gearbox model by applying a torque impulse at the input shaft and measuring the dynamic response. Numerical impulse test provides natural frequencies and mode shapes of the gearbox. Results of the impulse test are correlated with experimental measurements conducted by NASA personnel [44] and the Ohio State research group.

The frequency spectrum of dynamic transmission error and shaft displacement for the speed range from 0 to $8000\,Hz$ are shown in Figures 25(a) and 25(b). The computed natural frequencies agree with experiments as compared in Table 4. NASA accelerometers identify natural frequencies near 3000 to $4500\,Hz$, but the coherence is relatively low at

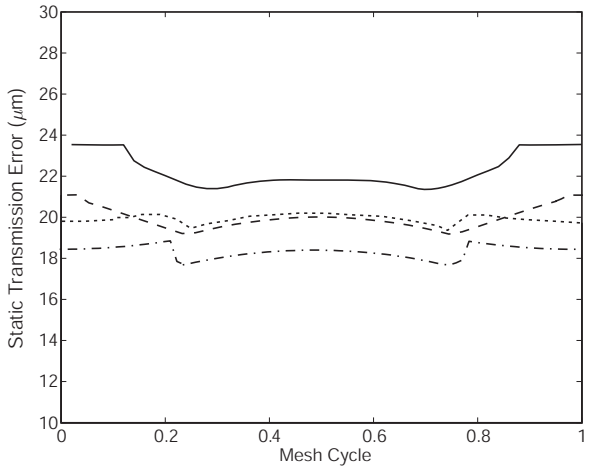

Figure 21: Static transmission error of the gear pair without the shaft and bearing compliance. The results are calculated by finite element ($-$), Program X ($- \cdot -$), NASA DANST ($\cdots$), and Load Distribution Program ($--$). The torque equals $79.09\,Nm$.

these higher frequencies. Measurements show several modes near $6500\,\text{to}\,7500\,Hz$ that are difficult to resolve, while simulations predict only one natural frequency at $6856\,Hz$. The mode shapes of these natural frequencies include mesh deflection modes, shaft modes, housing modes, and coupled modes.

Finite Element	Experiment
759	750
1942	2000
2195, 2283	2500
3803, 4449, 4654	3000-4500
6856	6500-7500

Table 4: Natural frequencies predicted by numerical impulse tests and measurements (Hz)

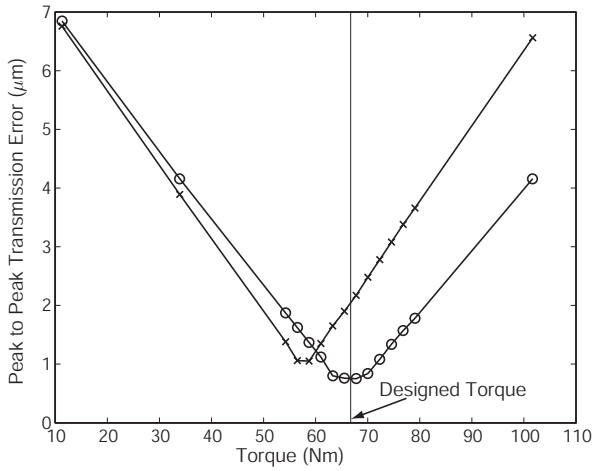

Figure 22: Peak to peak amplitude of static transmission error of the gear pair with $(- \times -)$ and without $(- \circ -)$ shafts at different torques.

5 Analytical Gearbox Dynamic Modeling and Analysis

Mathematical modeling of the gearbox provides fast dynamic analysis of the gearbox. Dynamic analysis, especially at multiple operating speeds, requires much computational effort using the finite element model. Analytical model gives the natural frequencies and mode shapes, and dynamic response at various operating speeds.

This analytical model employees crucial information on transmission error, mesh stiffness, bearing stiffness, and housing compliance from the finite element analysis.

5.1 The Gear Pair

The gear pair model is constructed following the literature [45, 46, 47, 48, 49, 50, 51], in which detail discussions into the validity of the modeling can be found. The model consists of two gears mounted on shafts. Each gear body is combined with its supporting shaft into a single rigid body. These gear-shaft bodies are each mounted on up two bearings placed at arbitrary axial locations. Figure 26 shows the gear model and the bases. A fixed, right-handed, orthonormal basis $\{\mathbf{E}\} = \{\mathbf{E}_1, \mathbf{E}_2, \mathbf{E}_3\}$ is oriented such that $\mathbf{E}_1$ is parallel to the line of action of the gear mesh. The origin is on the rotation axis of the pinion body, midway in the active facewidth. This dimensioning allows arbitrary axial positioning of meshing gears with different facewidth because any inactive facewidth is treated as part of

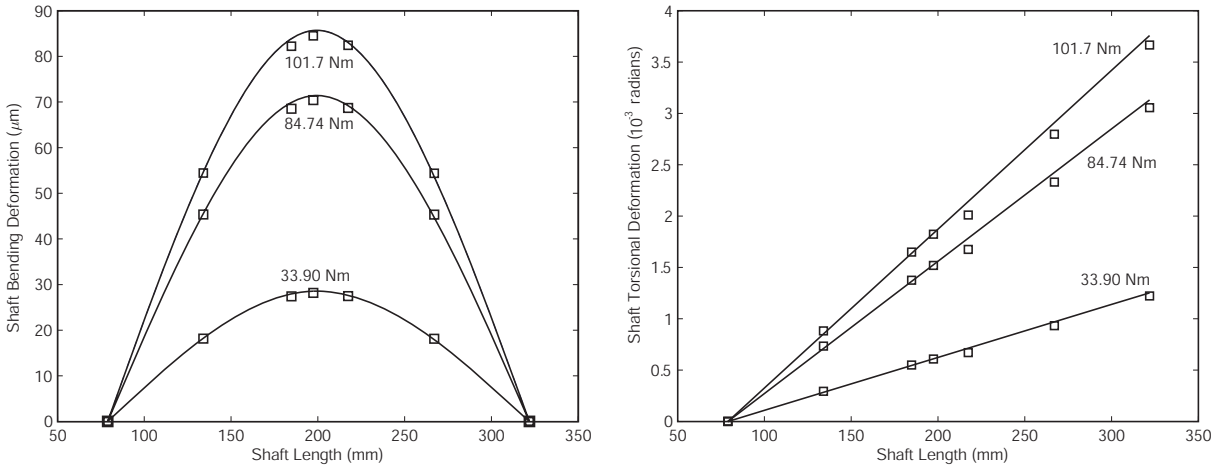

(a) (b)

Figure 23: (a) Input shaft bending deformation calculated by analytical beam theory (solid line) and finite element method (square marker) with simply-supported boundary conditions under various input torques; (b) Input shaft torsional deformation calculated by analytical beam theory (solid line) and finite element method (square marker) with clamped-free boundary conditions under various input torques. The shaft has uniform outer diameter ($30.23\,mm$).

the shaft. The translational (x_p, y_p, z_p) and angular (ϕ_p, θ_p, β_p) coordinates of the pinion body are assigned to translations along and rotations about $\mathbf{E}_1$, $\mathbf{E}_2$, and $\mathbf{E}_3$, respectively. The translational and angular coordinates of the gear body follow similarly with subscript g. Body-fixed bases $\{\mathbf{e}^p\} = \{\mathbf{e}_1^p, \mathbf{e}_2^p, \mathbf{e}_3^p\}$ and $\{\mathbf{e}^g\} = \{\mathbf{e}_1^g, \mathbf{e}_2^g, \mathbf{e}_3^g\}$ for the pinion and gear are adopted. Positive axial quantities are measured along $\mathbf{E}_3$ from the dashed line in Figure 26.

The pinion translational and angular velocity vectors are

$$\begin{aligned}
\dot{\mathbf{r}}_p &= \dot{x}_p\mathbf{E}_1 + \dot{y}_p\mathbf{E}_2 + \dot{z}_p\mathbf{E}_3, \\
\boldsymbol{\omega}_p &= \left[\dot{\phi}_p - \theta_p\left(\dot{\beta}_p + \Omega_p\right)\right]\mathbf{e}_1^p + \left[\dot{\theta}_p + \phi_p\left(\dot{\beta}_p + \Omega_p\right)\right]\mathbf{e}_2^p + \left[\dot{\beta}_p + \Omega_p - \phi_p\dot{\theta}_p\right]\mathbf{e}_3^p,
\end{aligned} \tag{4}$$

where Ω_p is the constant angular rotational speed of the pinion. The velocity vectors for the gear are identical except with components for the gear.

The pinion body is supported by two bearings at points A_p and B_p. The axial positions of these bearings measured along $\mathbf{E}_3$ are L_p^A and L_p^B. The pinion bearing deflection vectors at point A_p and B_p are the relative deflections of points A_p and B_p with respect to ground,

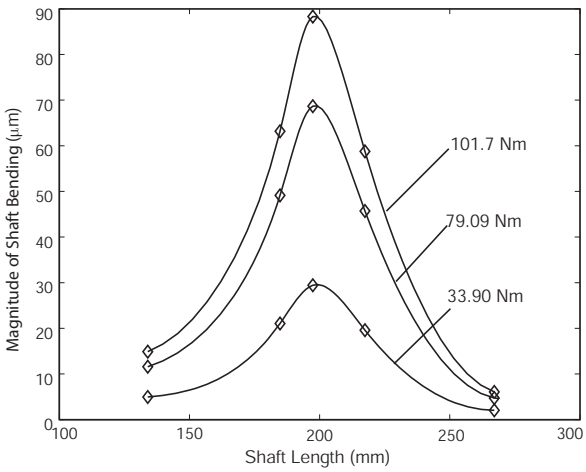

Figure 24: Shaft bending deformation under various input torques.

giving

$$\begin{aligned}\mathbf{d}_p^A &= \left[\theta_p\left(L_p^A - e_p\right) + x_p\right]\mathbf{E}_1 + \left[\phi_p\left(e_p - L_p^A\right) + y_p\right]\mathbf{E}_2 + z_p\mathbf{E}_3,\\ \mathbf{d}_p^B &= \left[\theta_p\left(L_p^B - e_p\right) + x_p\right]\mathbf{E}_1 + \left[\phi_p\left(e_p - L_p^B\right) + y_p\right]\mathbf{E}_2 + z_p\mathbf{E}_3.\end{aligned} \tag{5}$$

The bearing deflections for the gear follow similarly. The bearings resist tilting as well. The angular deflection of the pinion body bearing at A_p is

$$\boldsymbol{\gamma}_p^A = \phi_p\mathbf{E}_1 + \theta_p\mathbf{E}_2 + \beta_p\mathbf{E}_3. \tag{6}$$

The angular bearing deflection at point B_p is identical to Eq. (6) for rigid shafts. The bearings are isotropic in the $\mathbf{E}_1 - \mathbf{E}_2$ plane. At point A_p, the bearing stiffness matrix $\mathbf{K}_p^A$ as given in Eq. (1) is fully-populated, where the equality of stiffness in the two translation directions is evident. The bearing translational and angular displacements combined are $\boldsymbol{\Gamma} = \begin{Bmatrix}\mathbf{d}\\ \gamma\end{Bmatrix}$. Similar definitions follow for point B_p and for the gear body.

The gear mesh interface is modeled by a series of springs along the nominal lines of contact for no mesh deflection. These lines change as the gears rotate. Each spring acts at a point denoted by C_i. When the gear bodies deflect, the contact points on the pinion separate or compress against the contact points on the gear. The difference between the position vectors of the contact points on the pinion and gear gives the relative mesh deflection vector at C_i. The projection of the relative mesh deflection vector on the tooth surface normal gives the relative compressive deflection at the ith contact point. The

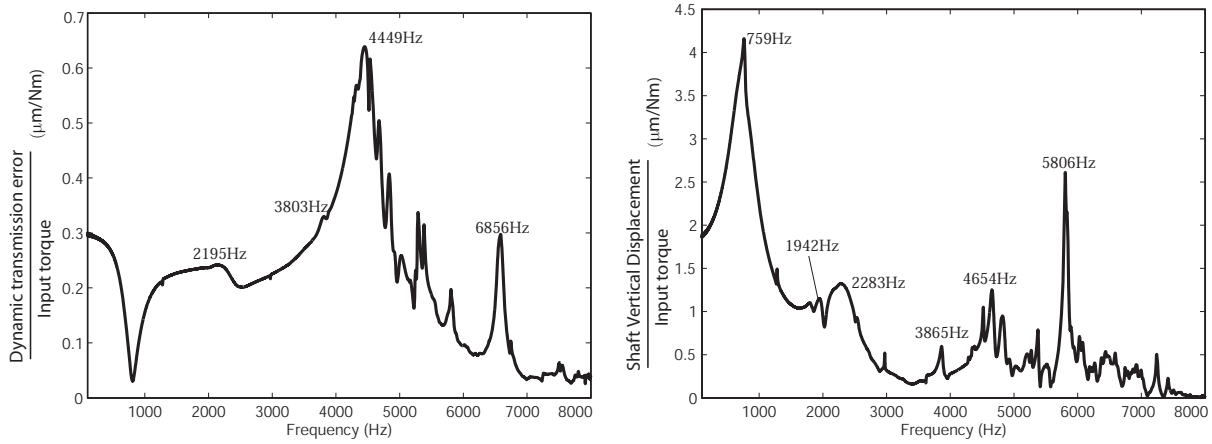

(a) (b)

Figure 25: Numerical impulse test results of (a) dynamic transmission error and (b) the input shaft horizontal displacement of the gear-bearing-housing system within speed range from $0\,Hz$ to $7000\,Hz$. The applied torque is $79.09\,Nm$.

relative compressive deflection is

$$\begin{aligned}\delta_i(\mathbf{q},t) = &\Big\{ [e_p - c_i(t)]\,\theta_p + [c_i(t) - e_g]\,\theta_g - x_p + x_g + h_i + \beta_p r_p + \beta_g r_g \Big\} \cos\psi \\ &- \Big\{ [b_i(t) + h_i]\,\theta_p + [(r_p + r_g)\,\theta_g \tan\Phi - b_i(t)] + z_p - z_g + \phi_p r_p + \phi_g r_g \Big\} \sin\psi,\end{aligned} \tag{7}$$

where r_p and r_g are the base radii, Φ is the transverse operating pressure angle, and ψ is the base helix angle. The vector $\mathbf{q}$ comprises generalized coordinates

$$\mathbf{q} = \Big(\underbrace{\phi_p, \theta_p, \beta_p, x_p, y_p, z_p}_{\text{pinion}}, \underbrace{\phi_g, \theta_g, \beta_g, x_g, y_g, z_g}_{\text{gear}} \Big) \tag{8}$$

The axial position of a contact point is $c_i(t)$ measured from the origin along $\mathbf{E}_3$, and the transverse position of a contact point is $b_i(t)$ measured from the origin along $-\mathbf{E}_1$. They are known functions of time determined by the contact line progressions as the gears rotate. Micron-level deviations of the tooth surface from an involute at any contact point i, such as from gear tooth surface modifications and manufacturing errors, are denoted by h_i. Figures 26 and 27(b) depict these quantities.

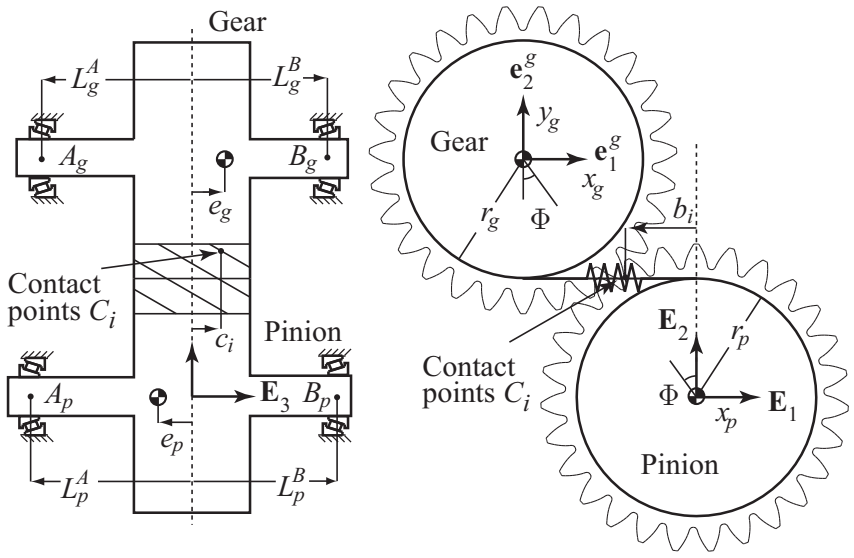

Figure 26: Analytical model of the gear pair. The parameters are defined in [7]. The dashed line is at the center of the active facewidth.

The kinetic and potential energies are

$$\begin{aligned} T &= \frac{1}{2}\left(\boldsymbol{\omega}_p^T \mathbf{J}_p \boldsymbol{\omega}_p + \boldsymbol{\omega}_g^T \mathbf{J}_g \boldsymbol{\omega}_g + \dot{\mathbf{r}}_p^T m_p \dot{\mathbf{r}}_p + \dot{\mathbf{r}}_g^T m_g \dot{\mathbf{r}}_g\right), \\ V &= \frac{1}{2}\left[\boldsymbol{\Gamma}_p^{A^T} \mathbf{K}_p^A \boldsymbol{\Gamma}_p^A + \boldsymbol{\Gamma}_p^{B^T} \mathbf{K}_p^B \boldsymbol{\Gamma}_p^B + \boldsymbol{\Gamma}_p^{A^T} \boldsymbol{K}_G^A \boldsymbol{\Gamma}_p^A + \boldsymbol{\Gamma}_p^{B^T} \boldsymbol{K}_G^B \boldsymbol{\Gamma}_p^B\right] \\ &\quad + \frac{1}{2}\sum_{i=1}^{n(t)} k_i(\mathbf{q},t)\delta_i(\mathbf{q},t)^2, \end{aligned} \tag{9}$$

where $k_i(\mathbf{q},t)$ is the ith contact stiffness, and $n(t)$ is the number of contact segments at an instant t. These quantities change as the gears rotate, hence the time dependence. The inertia tensor of the axisymmetric pinion body is $\mathbf{J}_p = \text{diag}\left[J_p^x, J_p^x, J_p^z\right]$ with similar definition for the axisymmetric gear body.

Lagrange's equations of motion for unconstrained generalized coordinates follow after substitution of equations Eqs. (4) through (7) into the energy expressions Eq. (9). In matrix form they are

$$\mathbf{M}_s \ddot{\mathbf{q}}_s + \mathbf{D}\dot{\mathbf{q}}_\mathbf{s} + \Omega_p \mathbf{G}_s \dot{\mathbf{q}}_s + \left[\mathbf{K}_\mathbf{s}(\mathbf{q},\mathbf{t}) - \Omega_p^2 \mathbf{C}_s\right]\mathbf{q} = \mathbf{F}(\mathbf{q},\mathbf{t})_s, \tag{10}$$

The vector $\mathbf{F}$ includes external loading; the driving and absorbing torques and tooth surface modifications h_i appear here. The matrix $\mathbf{K}$ represents the system elasticity with losses contained in the modal damping matrix $\mathbf{D}$. Tooth surface modifications h_i are neglected in $\mathbf{K}$ because $h_i \ll b_i(t)$, and the h_i appear as additions to $b_i(t)$. The terms that arise from

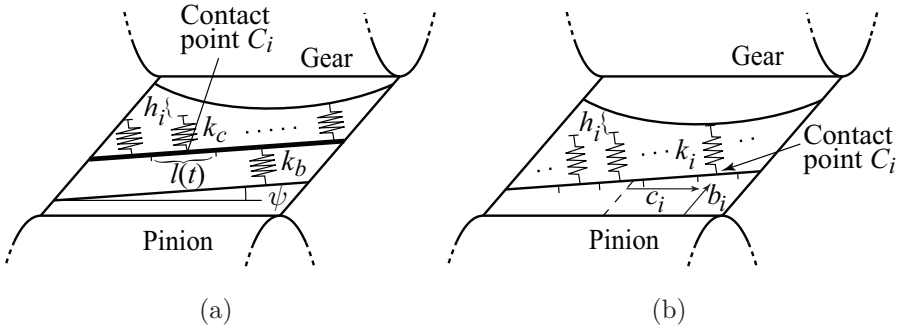

Figure 27: (a) Distributed spring network over a contact line with the local and bulk stiffnesses, $k_c l(t)$ and k_b. (b) Local $k_c l(t)$ and bulk k_b stiffnesses are combined into contact stiffness $k_i(\mathbf{q}, t)$ by Eq. (14).

the constant rotation speed are contained in the gyroscopic matrix $\mathbf{G}$ and the centripetal acceleration matrix $\mathbf{C}$. Individual elements of $\mathbf{M}$, $\mathbf{K}$, $\mathbf{G}$, $\mathbf{C}$, and $\mathbf{f}$ are given in [7].

Following [52, 50] the nominal contact lines are discretized into $n(t)$ segments of equal length $l(t)$, as shown in Figure 27(a). Each contact point C_i is positioned at the center of its segment. As the contact lines progress with gear rotation, the total number of segments $n(t)$ and the length of a segment $l(t)$ change. Each contact line has a specified number of segments. This discretization is based on the nominal lines of contact with no gear deflections.

Each contact spring is attached to its contact point C_i. The stiffness $k_i(\mathbf{q}, t)$ of contact springs are obtained by considering two separate categories of tooth deflection: local (ϵ_i) and bulk (δ_b). Discussion of this categorization can be found in [52, 49, 53]. The local deflection represents the Hertz contact deflections. The associated local stiffness is $k_c l(t)$, where the constant k_c is the local stiffness per unit contact length. The bulk deflection represents all deflections except local deflection, and those include gear blank deflection, tooth bending, shear, etc. Because the Hertz contact deflections are localized and far enough from the bulk deflections, the bulk deflection is assumed to be the same for all contact segments. The bulk stiffness k_b is assumed constant. The bulk spring is in series with the local springs, so the total deflection at the ith contact point C_i is

$$\delta_i = \epsilon_i + \delta_b \tag{11}$$

The mesh force F equals the sum of all forces carried by the local springs and also the

force carried by the bulk spring due to the series connection. The mesh force is

$$F = \sum_{i=1}^{n} F_i = k_c l(t) \sum_{i=1}^{n} \epsilon_i H(\epsilon_i) = k_b \delta_b, \tag{12}$$

$$H(\epsilon_i) = \begin{cases} 1; & \epsilon_i \geq 0 \\ 0; & \epsilon_i < 0 \end{cases} \tag{13}$$

is the Heaviside function that represents the contact condition at each contact spring. Use of Eqs. (11) and (12) reduce the network of local and bulk springs into $n(t)$ contact springs (k_i, $i = 1, 2, \ldots, n$) in parallel, as shown in Figure 27(b). The ith contact stiffness is given by

$$k_i(\mathbf{q}, t) = \frac{k_b k_c l(t) H(\epsilon_i)}{k_b + k_c l(t) \sum_{i=1}^{n(t)} H(\epsilon_i)}. \tag{14}$$

One can then calculate the ith potential energy $k_i \delta_i^2/2$ stored in the gear mesh in Eq. (9) from the contact force $F_i = k_i \delta_i$.

The local stiffness per unit length k_c and the bulk stiffness k_b are parameters of the gear pair determined by the contact mechanics and elasticity of the gears. These constants can be approximated analytically [52] or semi-analytically [50] by assigning certain types of stiffnesses such as Hertz contact, tooth bending, shear, etc. to k_c and k_b. A different approach is used in this work, where k_c and k_b are solved for from the deflections obtained from an external analysis tool for computational static analyses. In this case, k_c and k_b are numerical values that best fit the deflection obtained from finite element contact analysis of gears.

The following stipulations simplify the algebra to find k_c and k_b. 1) The tooth surface is perfectly involute, that is, $h_i = 0$ for all i; 2) All degrees of freedom are constrained to be zero except the pinion rotation β_p; and 3) A specified moment about $\mathbf{E}_3$ is applied to the pinion. With these stipulations, the deflections at all contact points are identical, that is, $\delta_i = \delta$ for all i in Eq. (7). Consequently, all points are in contact; $H_i = 1$ for all i. The subscript i of k_i is unnecessary because when all segments are in contact, $k_1 = k_2 = \ldots = k_n$. Use of static equilibrium, Eq. (11), and Eq. (14) gives

$$\delta(t) = F \left[\frac{1}{k_b} + \frac{1}{k_c L(t)} \right], \tag{15}$$

where $\delta(t)$ is the static transmission error, $L(t) = n(t) l(t)$ is the total contact line length at an instant t, and F is the constant mesh force obtained from the known applied torque. The two unknowns (k_c, k_b) are solved using the data from finite element analysis results

at two instances $\{\delta(t_1), L(t_1)\}$ and $\{\delta(t_2), L(t_2)\}$ within a mesh cycle. To increase accuracy, values at these two instances are calculated from averages of the four points where transmission error is highest (giving the values for the first instance) and the four points where transmission error is lowest (giving the values for the second instance).

The gear mesh model is validated by finite element analysis. Figure 28 shows transmission error comparison between the finite element and the analytical model for a helical and a spur gear pair.

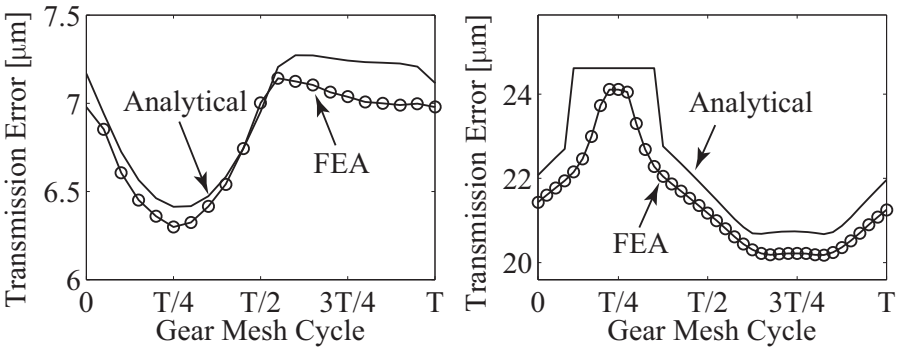

(a) (b)

Figure 28: Static transmission error from the analytical (solid line) and finite element (circles) model. (a) A helical gear pair. Quadratic tip relief starting at $\alpha = 28$ deg and root relief at $\alpha = 27$ deg. Tip relief, root relief, and circular lead crown are 10 μm. The applied torque is 200 N-m. (b) Spur gear pair in [8]. Linear tip relief starting at $\alpha = 23.6$ deg with amplitude 10 μm. Circular lead crown is 5 μm. The applied torque is 340 N-m.

5.2 Incorporating Housing Compliance with the Analytical Gear/Shaft Model

The equations of motion for the housing is given by

$$\mathbf{M}_H \ddot{\mathbf{q}}_H + \mathbf{K}_H \mathbf{q}_H = \mathbf{F}_H \tag{16}$$

where $\mathbf{M}_H$ and $\mathbf{K}_H$ are the mass and the stiffness matrices with degrees of freedom $\mathbf{q}_H$ and the force vector $\mathbf{f}_H$. Figure 29 helps explain the approach. The gear/shaft equations of motion are expanded by the addition of bearing degrees of freedom $\mathbf{q}_b$ and the housing equation of motion by Partitioning of (16) to separate the degrees of freedom where the

bearings are attached from the rest of the housing giving

$$\begin{bmatrix} \mathbf{M}_c & \mathbf{0} \\ \mathbf{0} & \mathbf{M}_h \end{bmatrix} \begin{pmatrix} \ddot{\mathbf{q}}_c \\ \ddot{\mathbf{q}}_h \end{pmatrix} + \begin{bmatrix} \mathbf{K}_c & \mathbf{K}_{ch} \\ \mathbf{K}_{ch}^T & \mathbf{K}_h \end{bmatrix} \begin{pmatrix} \mathbf{q}_c \\ \mathbf{q}_h \end{pmatrix} = \begin{pmatrix} \mathbf{f}_c \\ \mathbf{f}_h \end{pmatrix} \tag{17}$$

The new equations of motion are given by

$$\begin{bmatrix} \mathbf{M}_s & \mathbf{0} \\ \mathbf{0} & \mathbf{M}_b \end{bmatrix} \begin{pmatrix} \ddot{\mathbf{q}}_s \\ \ddot{\mathbf{q}}_b \end{pmatrix} + \begin{bmatrix} \mathbf{K}_s & \mathbf{K}_{sb} \\ \mathbf{K}_{sb}^T & \mathbf{K}_b \end{bmatrix} \begin{pmatrix} \mathbf{q}_s \\ \mathbf{q}_b \end{pmatrix} = \begin{pmatrix} \mathbf{f}_s \\ \mathbf{f}_b \end{pmatrix} \tag{18}$$

where, the matrix $\mathbf{K}_{sb}$ includes the coupling between the bearing degrees of freedom and the system. $\mathbf{M}_c$ and $\mathbf{K}_c$ are the mass and stiffness matrices, $\mathbf{q}_c$ is the degrees of freedom, and $\mathbf{f}_c$ is the force at the connection points. The bearing ends are massless, $\mathbf{M}_b = \mathbf{0}$.

The rest of the housing mass, stiffness, degrees of freedom and forcing are contained in $\mathbf{M}_h$, $\mathbf{K}_h$, $\mathbf{q}_h$, and $\mathbf{f}_h$. The connection between the bearings and the housing requires that at the interface displacements are equal, $\mathbf{q}_b = \mathbf{q}_c$, and the forces are transmitted $\mathbf{f}_b = -\mathbf{f}_c$. Eliminating $\mathbf{q}_c$ using these connection requirements gives

$$\begin{bmatrix} \mathbf{M}_s & \mathbf{0} & \mathbf{0} \\ \mathbf{0} & \mathbf{M}_b & \mathbf{0} \\ \mathbf{0} & \mathbf{0} & \mathbf{M}_h \end{bmatrix} \begin{pmatrix} \ddot{\mathbf{q}}_s \\ \ddot{\mathbf{q}}_b \\ \ddot{\mathbf{q}}_h \end{pmatrix} + \begin{bmatrix} \mathbf{K}_s & \mathbf{K}_{sb} & \mathbf{0} \\ \mathbf{K}_{sb}^T & \mathbf{K}_c + \mathbf{K}_b & \mathbf{K}_{ch} \\ \mathbf{0} & \mathbf{K}_{ch}^T & \mathbf{K}_h \end{bmatrix} \begin{pmatrix} \mathbf{q}_s \\ \mathbf{q}_b \\ \mathbf{q}_h \end{pmatrix} = \begin{pmatrix} \mathbf{f}_s \\ \mathbf{0} \\ \mathbf{f}_h \end{pmatrix} \tag{19}$$

This is the general form that connects the gears, shafts, and bearings to the full housing model which includes the flexibility as well as the inertia. If the housing inertia is neglected, i.e. static condensation, $\mathbf{M}_h = \mathbf{M}_b = \mathbf{0}$ and there are no external forces on the housing $\mathbf{f}_h = \mathbf{0}$, the last row of (19) becomes $\mathbf{q}_h = -\mathbf{K}_h^{-1}\mathbf{K}_{ch}^T\mathbf{q}_b$. Substitution of $\mathbf{q}_h$ into the second row of (19) gives $\mathbf{q}_b = -\left[\mathbf{K}_b + \mathbf{K}_c - \mathbf{K}_{ch}\mathbf{K}_h^{-1}\mathbf{K}_{ch}^T\right]^{-1}\mathbf{K}_{sb}^T\mathbf{q}_s$. Substitution of $\mathbf{q}_b$ into the first row of (19) gives

$$\mathbf{M}_s\ddot{\mathbf{q}}_s + \Big\{\mathbf{K}_s - \mathbf{K}_{sb}\big[\mathbf{K}_b + \underbrace{\mathbf{K}_c - \mathbf{K}_{ch}\mathbf{K}_h^{-1}\mathbf{K}_{ch}^T}_{\mathbf{K}_f}\big]^{-1}\mathbf{K}_{sb}^T\Big\}\mathbf{q}_s = \mathbf{0} \tag{20}$$

This equation incorporates the housing flexibility, without added degrees of freedom and the housing inertia, into the equations of motion of the gears, shafts, and bearings. To this end, the calculation of $\mathbf{K}_c$, $\mathbf{K}_{ch}$, and $\mathbf{K}_h$ separately is unnecessary. A shorter path can be taken by evaluating the housing stiffness $\mathbf{K}_f$ at the connection interface using influence coefficients of the housing (16). This is discussed in the following subsection.

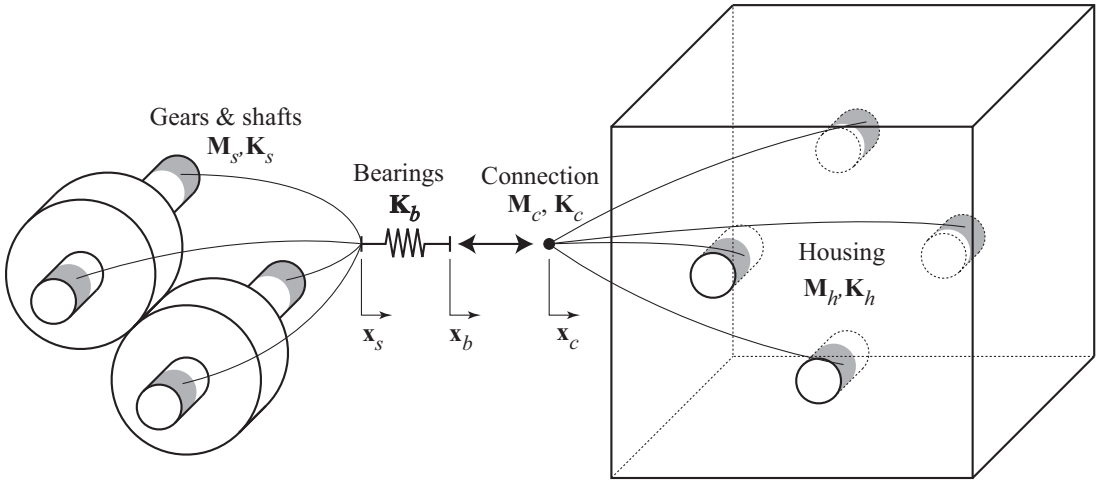

Figure 29: Description of the connection between the gears, shafts and bearings to the housing model.

5.2.1 Including the Housing by Using Influence Coefficients

The influence coefficient matrix $\mathbf{C}_f$ can be solved from (16) $\mathbf{C}_f\mathbf{f}_c = \mathbf{q}_c$ Solving for $\mathbf{q}_h$ from (17) gives

$$\mathbf{C}_f^{-1} = \mathbf{K}_f = \mathbf{K}_c - \mathbf{K}_{ch}\mathbf{K}_h^{-1}\mathbf{K}_{ch}^T \tag{21}$$

which allows use of the influence coefficient matrix in (20).

The procedure to obtain elements of $\mathbf{C}_f^{n\times n}$ consists of applying a unit force to each degree of freedom at the connection points $\mathbf{f}_c$ one at a time, and measuring the deflection of all the degrees of freedom at the connection points $\mathbf{q}_c$. Explicitly, elements in the i^{th} column, $\mathbf{C}_f^{<i><j>}$, are given by the displacements $\mathbf{q}_c^{<j>}$, calculated by (16) when there is a unit force at $\mathbf{f}_c^{<i>} = 1$, where $j = 1, \ldots, n$.

5.3 Dynamic Analysis Using the Analytical Model

Table 5 shows the natural frequencies of four systems: 1) cylindrical/ball bearings with housing flexibility, 2) wave bearings with housing flexibility, 3) cylindrical/ball bearings without housing flexibility, and 4) wave bearings without housing flexibility. Figure 30 shows the mesh deflection mode from the analysis with cylindrical/ball bearings with housing flexibility. The mesh deflection mode is an important mode because the tooth pass excitation excites primarily the mesh deflection mode. This mesh deflection mode is demonstrated in experiments, which is strongly excited by the 2^{nd} harmonic of tooth pass frequency at $4200rpm$. This mode shows up strongly in our vibration speed maps. It is

highlighted in Table 5. The mesh deflection mode persists when bearing type is changed, and when the housing flexibility is included.

Linear dynamic analysis is performed using the mean system stiffness matrix obtained by averaging the quasi-static time-dependent system stiffness over a mesh period. The harmonic excitation is approximated from the first ten harmonics of the quasi-static displacement vector. Figure 31 shows the dynamic peak-to-peak transmission error from the four systems mentioned above. All systems have similar dynamic transmission error. Figure 32 shows the dynamic bearing reactions of the four systems. Wave bearings seem to produce higher dynamic bearing loads. Use of the housing flexibility moves the natural frequencies and thus the resonant peaks, but does not alter the peak amplitudes in a significant manner.

Cylindrical Roller		Ball Bearing	
With Housing	*Without Housing*	*With Housing*	*Without Housing*
576.6	975.5	875.2	2279
954.6	1000	1988	2535
987.7	1597	2246	3173
1515	1711	2387	3209
1599	1868	2749	3480
1793	1977	3003	3549
1915	2736	3150	**3982**
2075	2848	3373	4383
2356	**3910**	3514	4473
2722	-	**3957**	-
3893	-	4392	-

Table 5: Natural frequencies of the NASA gearbox with cylindrical roller/ball bearings, wave bearings, with housing flexibility and without housing flexibility. The mesh deflection mode natural frequencies are highlighted.

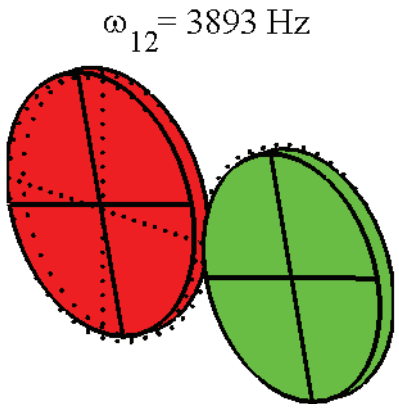

Figure 30: Graphical representation of the 12th mode at 3893 Hz (mesh deflection mode) from the system with ball/cylindrical bearings with housing.

6 Acoustic Radiation Gearbox Modeling and Analysis

The boundary element model of the gearbox housing is shown in Figure 33. This model includes 50,401 tetrahedron elements. Each element has nearly uniform length in order to have good aspect ratio. This model uses the fast multipole method (detailed in [32]) to calculate the gearbox sound radiation. This method provides fast acoustic calculation with a realistic system modeling. Given the complexity of housings, the great increase in the number of degrees of freedom admits solutions for realistic models not possible with conventional boundary element software. This method is implemented in Coustyx [19].

6.1 Model Validation and Mesh Convergence Study

This boundary element model of the gearbox has been validated against theoretical solutions of the sound field with a monopole. A monopole is a source which radiates sound equally well in all directions. The simplest example of a monopole source would be a sphere whose radius alternately expands and contracts sinusoidally. The far-field pressure radiated by a monopole may be written as

$$p(r,\theta,t) = \frac{iQ\rho ck}{4\pi r} e^{i(\omega t - kr)} \tag{22}$$

where ρ is the fluid density, c is the speed of sound, k is the wave number, ω is the frequency, and r is the local distance from source. Q is the complex source strength, which

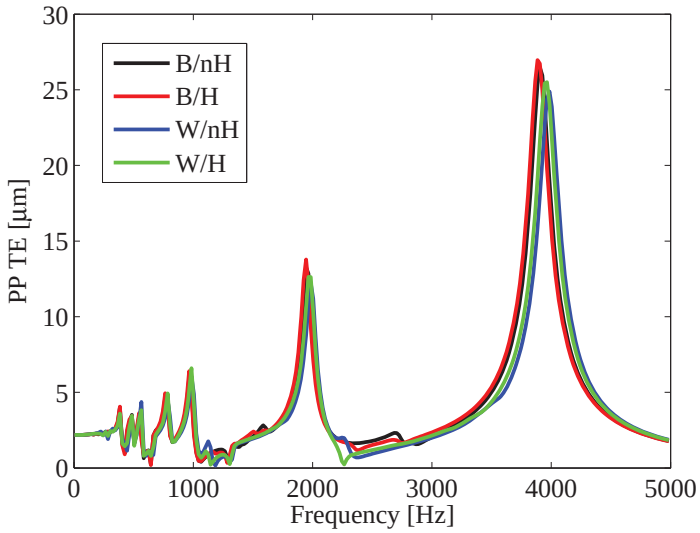

Figure 31: Peak-to-peak dynamic transmission error of four systems. Analysis with roller element bearings are marked by B, analysis with wave bearings are marked by W, analysis including the housing flexibility is marked by H, analysis without the housing is marked by nH.

is a constant number defined in [54].

The sound field excited by a monopole is not affected by the gearbox geometry, which allows simulation results to be compared against the theoretical solution of a monopole for an arbitrary geometry. In other words, the noise radiation from the gearbox surface equals to the theoretical solution of a monopole in the free space (shown in Figure 34). The velocity field caused by the point source (monopole) in free space at gearbox surface is calculated theoretically and used as the boundary condition for the actual housing model.

Optimal element length has been carefully chosen through mesh convergence study. The relative error of the computed pressure compared to the theoretical value in (22) with various element length is shown in Figure 35. Result accuracy is improved when element length is small. However, when element length is smaller than $8.636\,mm$, the result accuracy is disrupted as round off error becomes significant. The optimal element length is between $8.890\,mm$ and $10.16\,mm$ with less than 2% relative error. The mesh convergence study is important as the element length affects the solution accuracy.

Sound pressure of the radiated noise calculated by Coustyx and the theoretical solution is compared in Figure 36 for the speed range from 500 to $3500\,Hz$ using $9.000\,mm$ element length. Excellent agreement is present.

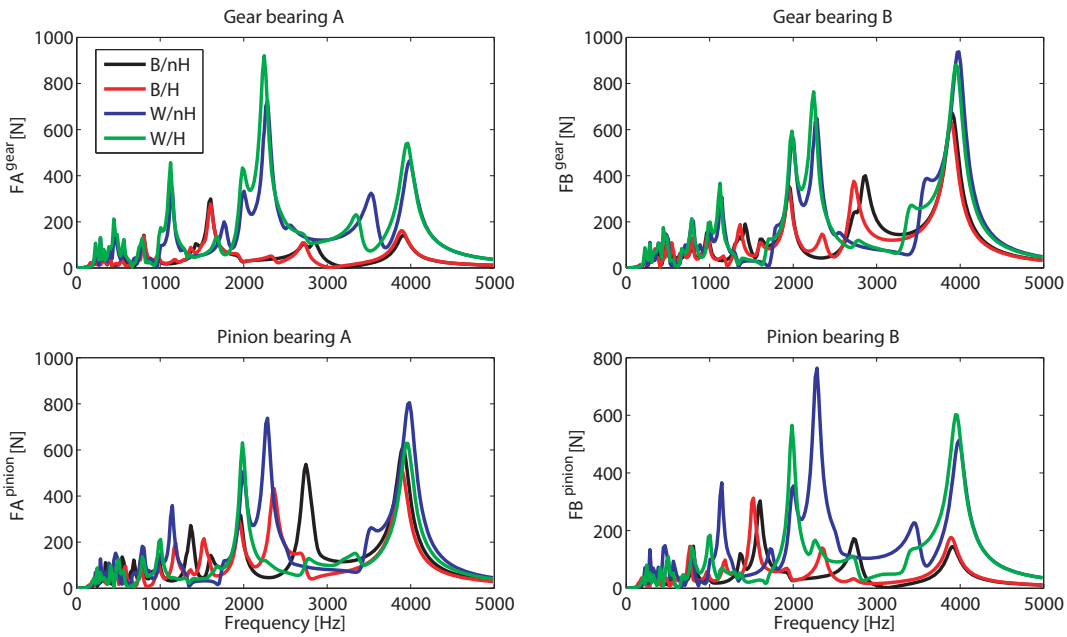

Figure 32: Dynamic bearing forces. Analysis with roller element bearings are marked by B, analysis with wave bearings are marked by W, analysis including the housing flexibility is marked by H, analysis without the housing is marked by nH.

6.2 Sound Pressure and Power Computation Using Transfer Functions

The computation of sound pressure and power of the radiated gearbox noise uses a network of transfer functions from unit bearing loads to sound pressure. Transfer functions describe the noise radiation property of the gearbox housing. The computation of these transfer functions is independent of the vibration analysis of the bearing reaction forces. Thus, these transfer functions are applicable for any type of bearings or gears.

The procedure to calculate transfer functions consists of applying a unit dynamic force to each degree of freedom $(x, y, z, \theta_x, \theta_y, \theta_z)$ at every bearing one at a time in the finite element model, measuring the velocity at the gearbox surface for various speeds in the finite element housing model, and computing the sound pressure of the radiated noise at specified locations in the gearbox environment using the computed velocity as the boundary condition in the boundary element model. Figure 37 shows a few calculated transfer functions at four different bearings. Sound pressure at arbitrary locations outside the gearbox is determined by the superposition of these transfer functions and multiplying the

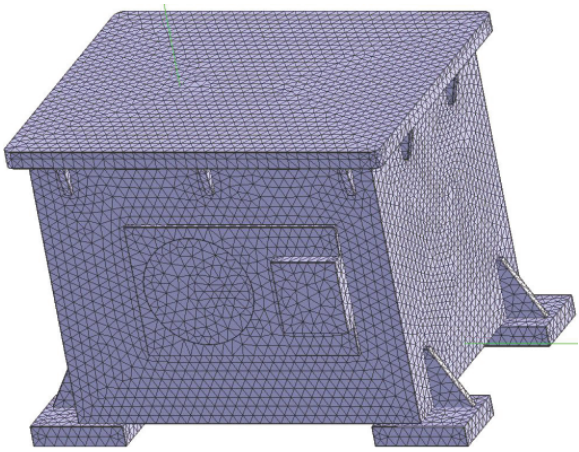

Figure 33: Boundary element model of the gearbox established in Coustyx.

fluctuating amplitudes of dynamic bearing forces at each degree of freedom of individual bearings.

Sound power is a better measure of the gearbox noise than sound pressure as it is independent of the geometric locations where noise is measured. Sound power measurements in experiments, however, require much effort. This study calculates the sound power using the aforementioned transfer functions.

To obtain accurate estimate of sound power, many numerical microphones are outside the gearbox. Those microphones are mounted on a measurement surface enveloping the gearbox, in this study, a sphere. According to the international standard ISO 3745, 20 microphones are used. The sound power is computed by integrating the sound pressure at these "microphones" in the sphere.

The sound power level, L_w is computed as:

$$\begin{aligned} L_w &= L_p + 10log_{10}(\frac{s}{s_0})(\text{in dB}) + c_1 + c_2 \\ c_1 &= -10log_{10}[\frac{B}{B_0}(\frac{313.15}{273.15+\theta})^{0.5}](\text{in dB}) \\ c_2 &= -15log_{10}[\frac{B}{B_0}(\frac{296.15}{273.15+\theta})^{0.5}](\text{in dB}) \end{aligned} \tag{23}$$

where s is the area of the measurement surface and $s_0 = 1\,m^2$. B is the barometric air pressure during measurements, in Pascals; B_0 is the reference barometric pressure. θ is the air temperature during measurement. L_p is the weighed surface sound pressure level

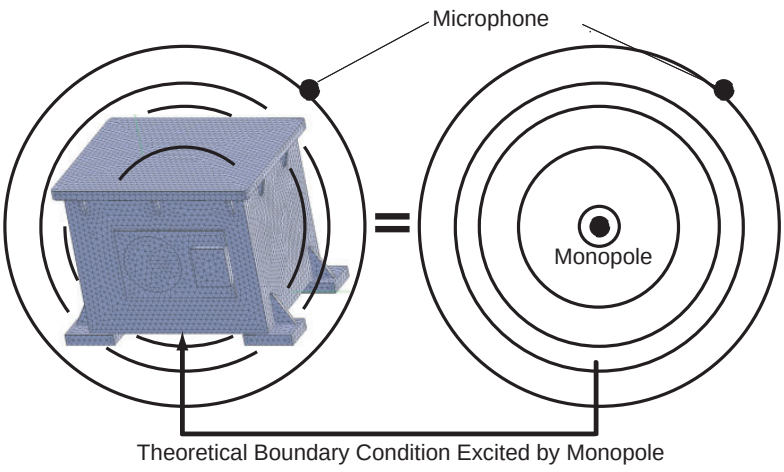

Figure 34: Theoretical solutions used to validate the boundary element housing model. Noise radiated from the housing with monopole velocity field at the gearbox surface as the boundary condition equals to that with monopole in the free space.

over the measurement surface in decibels.

$$L_p = 10log_{10}\{(\frac{1}{N}[\sum_i 10^{0.1(L_{p,i}+W)}])\}\text{in dB}$$
$$L_{p,i} = 20log_{10}(\frac{p_i}{p_0}) \tag{24}$$

where N is the number of microphone positions. W is the weighting function applied by the filter at the frequency of analysis. p_i is the root mean square pressure in Pa and $p_0 = 2 \times 10^{-5}\, Pa$.

6.3 Radiated Noise Correlation with Measurements

The calculated noise is compared against the measurements taken at NASA GRC gearbox. Two microphones are mounted to measure sound pressure in experiments at 790 mm directly above the gearbox, and are separated horizontally by 180 mm as shown in Figure 38.

Here, only the noise transmitted through rolling element bearings are compared against measurements because experimental data on sound pressure with wave bearings is not available. Figure 39 shows the time averages of the mean squared sound pressure $(p)^2_{av} = \sum_b (p_b)^2_{av}$ at microphone 1 estimated by measurements and computed, where ${(p_b)_{av}}^2$ is the addictive measure of sound pressure associated with the frequency band b from 0 to

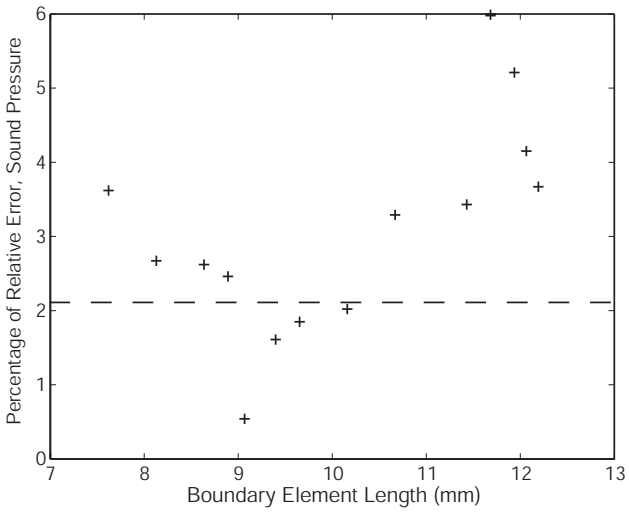

Figure 35: Effects of boundary element length on the relative error of calculated sound pressure compared to the theoretical solution.

$8000\,Hz$. For each gear mesh frequency, two different experimental results are shown: the minimum sound pressure including only mesh frequency harmonics; and the maximum sound pressure including mesh frequency harmonics and other frequency components. These frequencies are the side bands caused by the shaft rotation frequency, belt splice pass frequency, etc. The simulated sound pressure is within the experimental data range.

Figure 40 shows the frequency spectrum of the measured and simulated sound pressure when mesh frequency equals $2000\,Hz$. Good agreement is evident between the measurements and simulations at mesh frequency harmonics. Sidebands around the mesh frequency harmonics are present in the measured data. These sidebands are not included in the computational model because the causes are not known. Including these sidebands in the vibration/acoustics model would provide better agreement with the measurements.

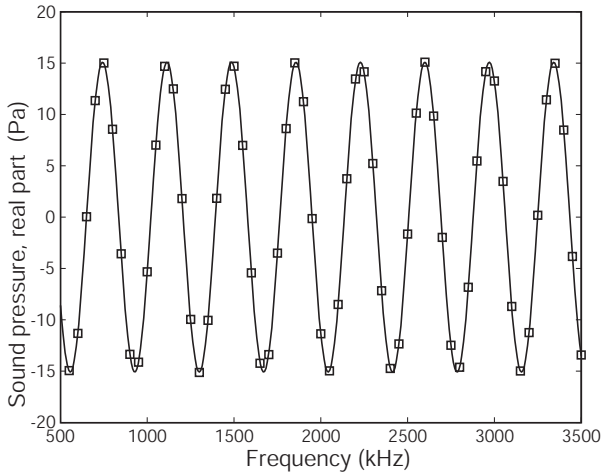

Figure 36: Sound pressure at the NASA microphone 1 location calculated by Coustyx (□) and theoretical models (−).

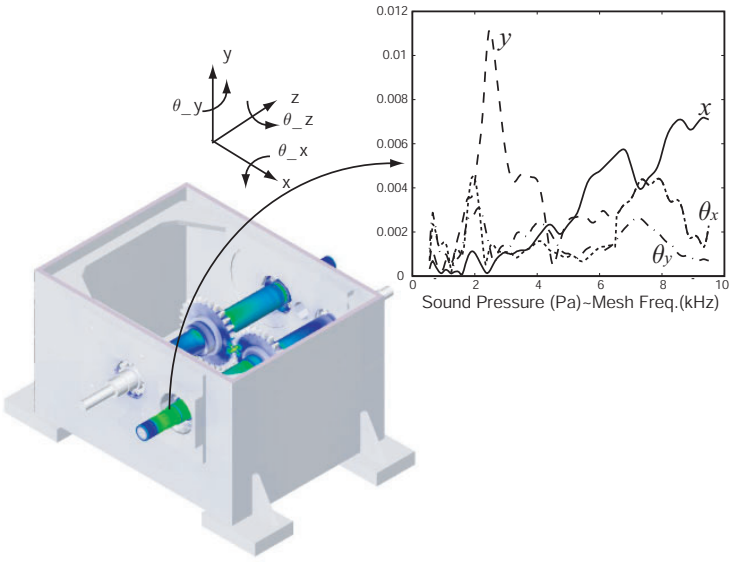

Figure 37: Sound pressure transfer functions when unit dynamic loads are applied at bearings. Six transfer functions are generated per each bearing along $x, y, z, \theta_x, \theta_y, \theta_z$ directions. The input torque is $79.09\,Nm$.

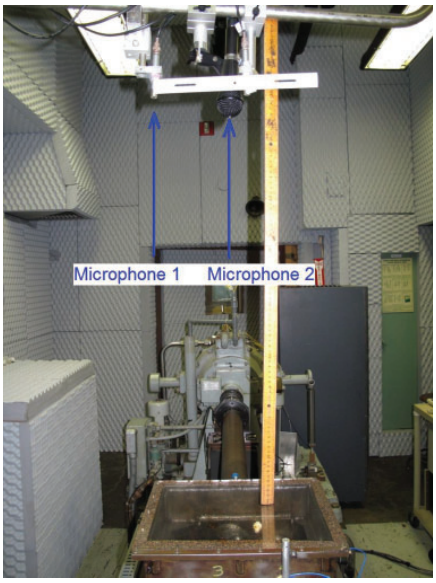

Figure 38: Microphones (1 and 2) mounted above the NASA GRC gearbox.

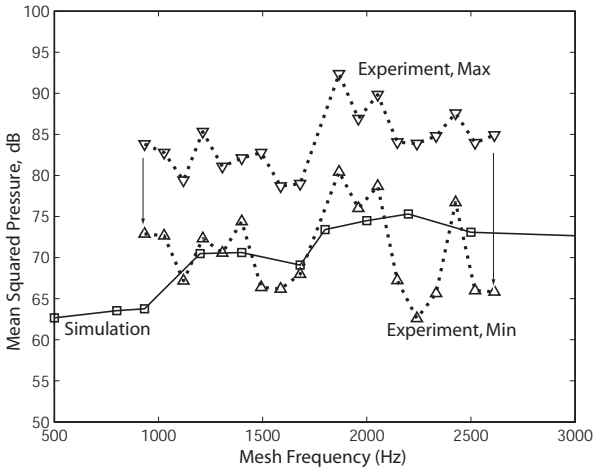

Figure 39: The time average of the experimental $(--)$ and calculated $(-)$ mean squared sound pressure at the microphone 1 location within mesh frequency range from 500 to 3000 Hz. The applied torque is 79.09 Nm.

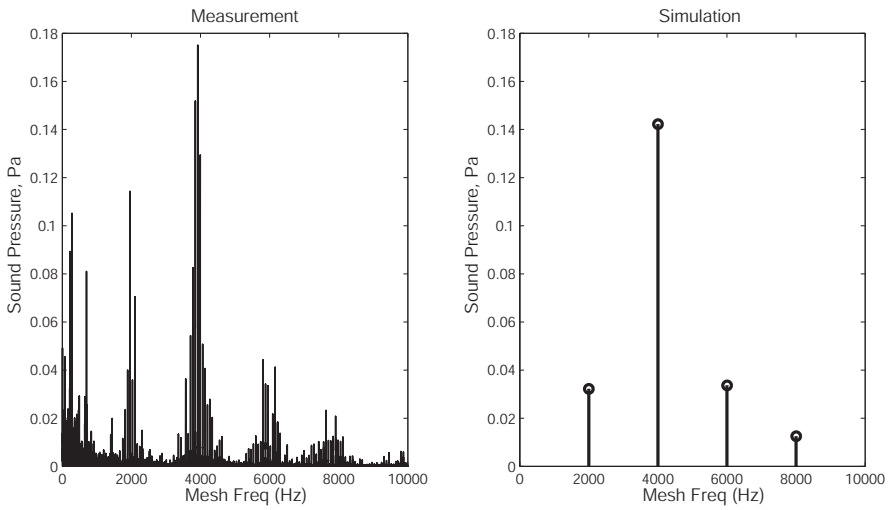

Figure 40: Frequency spectrum of the measured (left) and simulated (right) sound pressure at the microphone 1 location when mesh frequency is 2000 Hz. The applied torque is 79.09 Nm.

6.4 Noise Radiation Properties with Different Bearings

This section investigates the effectiveness of fluid film wave bearings in reducing noise. To that end, sound pressure and power of the radiated noise are compared between fluid film wave and rolling element bearings.

Sound pressure at the microphone 1 location excited by the first (left) and second (right) mesh frequency harmonics is compared between rolling element and wave bearings in Figure 41. The sound pressure of wave bearings is generally higher than with rolling element bearings. The difference is frequency dependent. When the second mesh frequency harmonic is near 3803 Hz (dominant mesh deflection mode), sound pressure with rolling element bearings is similar in shape and amplitude to that with wave bearings. The noise radiation is independent of bearing types at this frequency.

The sound power radiated from the gearbox is also compared between wave and rolling element bearings in Figure 42. The sound power level of the gearbox with rolling element and wave bearings is also speed-dependent. The radiated gearbox sound power with rolling element bearings is lower than that with fluid film wave bearings in general within the speed range of interest. There is no obvious benefit to replace rolling element bearings with wave bearings to reduce the gearbox noise within the speed range of interest, given the two dimensional wave bearing model used [38, 39].

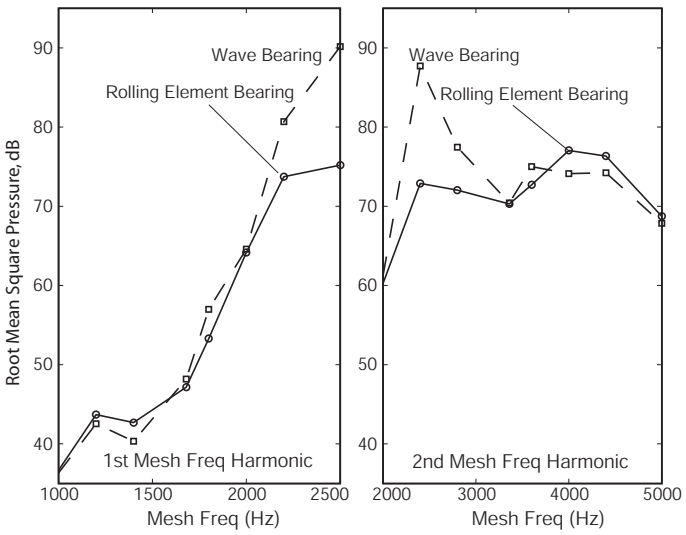

Figure 41: The frequency spectrum of the measured (left) and computed (right) sound pressure at the microphone 1 location when mesh frequency is between $1000\,Hz$ and $2500\,Hz$. The applied torque is $79.09\,Nm$.

7 Summary and Conclusions

This work investigates noise radiation from a gearbox with different types of bearings. A multi-dynamics model of the examined gearbox is established to address the vibro-acoustic propagation of the gear dynamics. It includes: 1). full fidelity finite element gearbox model; 2). lumped-parameter gearbox model; 3) finite element housing model; and 4). boundary element housing model. The procedure of the noise radiation analysis consists of: a). dynamic bearing force computation using the finite element and analytical gearbox models; b). gearbox surface velocity estimate with excitations from dynamic bearing forces obtained from a); and c). acoustic analysis of the gearbox with the boundary condition of the surface velocity calculated from b).

The full fidelity finite element/contact mechanics model of the NASA gearbox has been validated. Gear transmission error is compared among commercial software and matches the design objective. The rolling element and gear contact properties have been validated against experiments in the literature. Modal analysis has been performed on the entire gearbox model and results agree with measurements. The simplified lumped-parameter model of the gearbox is suitable for parametric studies on the dynamic response. The analytical model has been validated against the finite element analysis.

Cross-coupling stiffnesses are significant as they affect the gearbox dynamics. A fully-

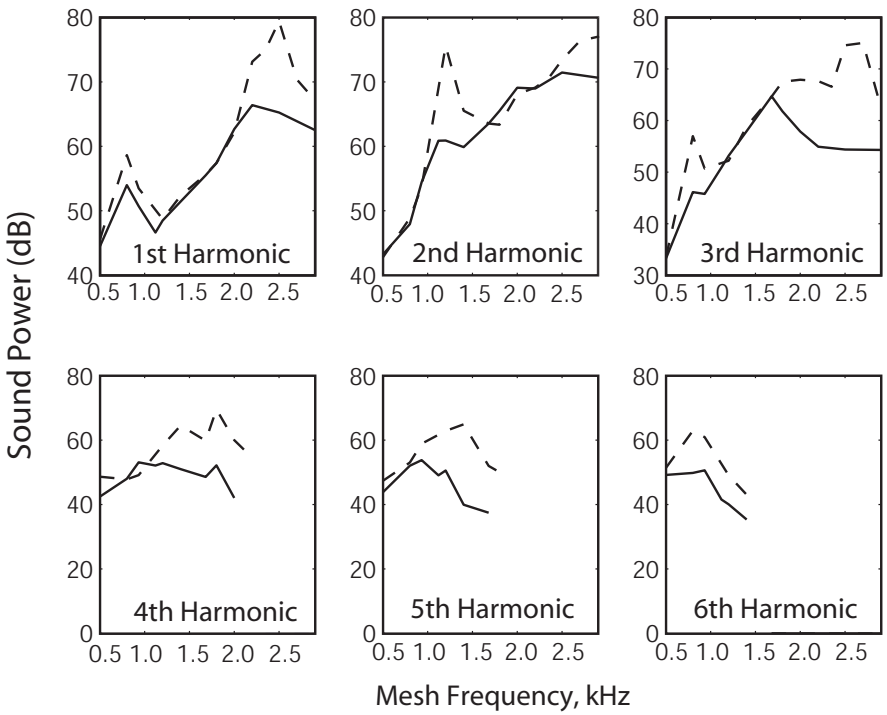

Figure 42: Sound power of radiated gearbox noise excited by certain mesh frequency harmonics of bearing forces with rolling element (−) and fluid film wave bearings (−−) at 79.09 Nm input torque. The excitation from 1^{st} to 6^{th} mesh frequency harmonics of bearing forces are considered during the computation. A weighing filter (ISO standard) is used to adjust sound pressure levels.

populated stiffness matrix is needed to fully represent rolling element bearings. Bearing stiffnesses fluctuate periodically as rolling elements enter and leave the region of loaded rollers. These stiffness variations could excite gearbox vibration.

This acoustic model has been validated by comparing against theoretical solutions and measurements taken at the NASA GRC gearbox. The transfer function method determines sound pressure and power for arbitrary bearings, which is exceptionally suitable for the gearbox optimization study to reduce noise. Noise radiation property of fluid film wave bearings is speed-dependent, and wave bearings are not superior to rolling element bearing in reducing gearbox noise. An one-way vibro-acoustic pass of the gearbox is present at the mesh deflection mode. Gear dynamics significantly affects the housing vibration and noise radiation. Housing and bearings, however, have limited effects on the gear vibration.

References

[1] Harris, T. A., 1990. *Rolling bearing analysis*, 3rd ed. John Wiley and Sons, Inc.

[2] Gargiulo, Jr., E. P., 1980. "A simple way to estimate bearing stiffness". *Mechine Design*, pp. 107–110.

[3] While, M. F., 1979. "Rolling element bearing vibration transfer characteristics: Effect of stiffness". *Journal of Applied Mechanics,* **46**, pp. 677–684.

[4] Royston, T. J., and Basdogan, I., 1998. "Vibration transmission through self-aligning (spherical) rolling element bearings: Theory and experiment". *Journal of Sound and Vibration,* **215**(5), pp. 997–1014.

[5] Kraus, J., Blech, J. J., and Braun, S. G., 1987. "In situ determination of rolling bearing stiffness and damping by modal analysis". *Journal of Vibration, Acoustics, Stress, and Reliability in Design,* **109**, pp. 235–240.

[6] Seybert, A. F., Wu, T. W., and Atherton, W., 1992. "Comparison of analysis and experiment for gearbox noise". *NASA Technical Memorandum 251523.* National Aeronautic and Space Administration, Cleveland Lewis Reseach Center.

[7] Eritenel, T., and Parker, R. G., 2011. "An investigation of tooth mesh nonlinearity and partial contact loss in gear pairs using a lumped-parameter model". *Mechanism and Machine Theory.* Submitted.

[8] Kahraman, A., and Blankenship, G. W., 1999. "Effect of involute tip relief on dynamic response of spur gear pairs". *Journal of Mechanical Design,* **121**(1), Mar., pp. 112–118.

[9] Mucchi, E., and Vecchio, A., 2010. "Acoustical signature analysis of a helicopter cabin in steady-state and run up operational conditions". *Measurement,* **43**, p. 283293.

[10] Hoffmann, F., Maier, R., Janker, P., Hermle, F., and Berthe, A., 2006. "Helicopter interior noise reduction by using active gearbox structs". *in: Proceedings of the 12th AIAA/CEAS Aerospace Conference*, May. Massachusetts, Cambridge.

[11] Dozio, L., Corbetta, W., Vigono, E., Forghieri, A., Ghiringhelli, G., and Cenedese, F., 2006. "Active solutions for the reduction of the transmission of structure-borne noise to the cabin structure on a a109 mockup". *Proceedings of ISMA*, September. Leuven, Belgium.

[12] Viswamurthy, S., and Ganguli, R., 2004. "An optimization approach to vibration reduction in helicopter rotors with multiple active trailing edge flaps,". *Aerospace Science and Technology,* **8**(3), p. 185194.

[13] Hirsch, S., Jayachandran, V., and Sun, J. Q., Composite Structures. "Structural-acoustic control for quieter aircraft interior-smart trim technology". *1998,* **42**(2), p. 189202.

[14] Randall, R., 2004. "Detection and diagnosis of incipient bearing failure in helicopter gearboxes". *Engineering Failure Analysis II*, p. 177 190.

[15] He, S., Singh, R., and Pavic, G., 2008. "Effect of sliding friction on gear noise based on a refined vibro-acoustic formulation". *Journal of Noise Control Engineering,* **56**(3), pp. 164–175.

[16] Lim, T. C., and Singh, R., 1991. "Statistical energy analysis of a gearbox with emphasis on the bearing path". *Journal of Noise Control Engineering,* **37**(2), pp. 63–69.

[17] Lim, T. C., and Singh, R., 1989. "A review of gear housing dynamics and acoustic literature". *NASA Contractor Report 185148.*

[18] Vijayakar, S. M. *Calyx User's Manual.* Advanced Numerical Solutions LLC, Hilliard, Ohio, 43026 USA. http://www.ansol.us/Manuals/Helical3DManual.pdf.

[19] *http://www.ansol.us/Products/Coustyx.*

[20] Dimofte, F., 1995. "Wave journal bearing with compressible lubricant; part i: The wave bearing concept and a comparison to the plain circular bearing". *STLE Tribology Transaction,* **38**(1), p. 153160.

[21] Dimofte, F., and Addy, Jr., H. E., 1994. "Preliminary experimental results of a three wave journal air bearing". *Proceedings of Advanced Earth-to-Orbit Propulsion Technology Conference,* **11**, May, p. 375384.

[22] Dimofte, F., Proctor, M. P., Fleming, D. P., and Keith, Jr, T. G., 2000. "Wave fluid film bearing tests for an aviation gearbox". *NASA Techanical Report,* **NASA/TM2000-209766**, Jan.

[23] Dimofte, F., 1995. "Wave journal bearing; part i: Analysis". *NASA Contractor Report 195431.*

[24] Hambric, S. A., Hanford, A. D., Shepherd, M. R., Campbell, R. L., and Smith, E. C., 2010. "Rotorcraft transmission noise path model, including distributed fluid film bearing impedance modeling". *NASA Technical Report.* Contract No. NNC08CB07C.

[25] Parker, R. G., Agashe, V., and Vijayakar, S. M., 2000. "Dynamic response of a planetary gear system using a finite element/contact mechanics model". *Journal of Mechanical Design,* **122**(3), Sept., pp. 304–310.

[26] Parker, R. G., Vijayakar, S. M., and Imajo, T., 2000. "Non-linear dynamic response of a spur gear pair: Modelling and experimental comparisons". *Journal of Sound and Vibration,* **237**(3), Oct., pp. 435–455.

[27] Ambarisha, V. K., and Parker, R. G., 2007. "Nonlinear dynamics of planetary gears using analytical and finite element models". *Journal of Sound and Vibration,* **302**, pp. 577–595.

[28] Bahk, C.-J., and Parker, R., 2011. "Analytical solution for the nonlinear dynamics of planetary gears". *ASME Journal of Computational and Nonlinear Dynamics,* **6**(2), p. 021007.

[29] Liu, G., and Parker, R. G., 2008. "Dynamic modeling and analysis of tooth profile modification of multi-mesh gears". *ASME Journal of Mechanical Design,* **130**, pp. 121402–1.

[30] Liu, G., and Parker, R. G., 2008. "Impact of tooth friction and its bending effect on gear dynamics". *Journal of Sound and Vibration,* **320**(4-5), Mar., pp. 1039–1063.

[31] Guo, Y., and Parker, R. G., 2010. "Stiffness matrix calculation of rolling element bearings using a finite element/contact mechanics model". *Mechanism and Machine Theory.* Submitted.

[32] Gunda, R., 2008. "Boundary element acoustics and the fast multipole method (fmm)". *Sound and Vibration*, March.

[33] Oswald, F. B., Townsend, D. P., Valco, M. J., Spencer, R. H., Drago, R. J., and Lenski, J. W., 1994. Influence of gear design parameters on gearbox radiated noise. Tech. Rep. ARL TR-381, NASA.

[34] Greogory, R. W., Harris, S. L., and Munro, R. G., 1963. "Dynamic behavior of spur gears". *Proceedings of the institution of mechanical engineers,* **178**, pp. 261–266.

[35] Vijayakar, S. M., 1991. "A combined surface integral and finite element solution for a three-dimensional contact problem". *International Journal for Numerical Methods in Engineering,* **31**, pp. 524–546.

[36] Liu, G., and Parker, R., 2008. "Nonlinear dynamics of idler gearsets". *Nonlinear Dynamics,* **53**, pp. 345–367.

[37] Guo, Y., and Parker, R. G., 2011. "Dynamic analysis of planetary gears with bearing clearance". *ASME Journal of Computational and Nonlinear Dynamics*. Submitted.

[38] Hanford, A., 2009. *Wave Journal Bearing Dynamic Coefficients Users Manual*. ARL/Penn State.

[39] Campbell, R. L. a., 2003. "Distributed journal bearing dynamic coefficients for structural finite element models". *Proceedings of ASME IMECE*. NCA-43770.

[40] Jones, A. B., 1946. "Analysis of stresses and deflections". *New Departure Engineering Data*. General Motors.

[41] Palmgren, A., 1959. *Ball and roller bearing engineering*. S. H. Burbank, Philadelphia,.

[42] Brandlein, J., Eschmann, P., Hasbargen, L., and Weigand, K., 1999. *Ball and roller bearings: theory, design and application*. John Wiley and Sons.

[43] Oswald, F. B., Lin, H. H., and Delgado, I. R., 1996. "Dynamic analysis of spur gear transmissions (danst)". *NASA Technical Memorandum 107291*. Technical Report ARLTR1189.

[44] Guo, Y., Parker, R. G., Eritenel, T., and Ericson, T. M., 2011. Vibration propagation of gear dynamics in a gear-bearing-housing system using mathematical modeling and finite element analysis. Tech. rep., NASA Contract NNC08CB03C.

[45] Blankenship, G. W., and Singh, R., 1995. "Dynamic force transmissibility in helical gear pairs". *Mechanism and Machine Theory,* **30**(3), Apr., pp. 323–339.

[46] Blankenship, G. W., and Singh, R., 1995. "A new gear mesh interface dynamic model to predict multi dimensional force coupling and excitation". *Mechanism and Machine Theory,* **30**(1), Jan., pp. 43–57.

[47] Salzer, M., Smith, J., and Welbourn, D., 1977. "Simulation of noise from gears when varying design and manufacturing parameters". *Proceedings of the World Congress on Gearing,* **1**, pp. 297–308.

[48] Kahraman, A., 1993. "Effect of axial vibrations on the dynamics of a helical gear pair". *Journal of Vibration and Acoustics,* **115**(1), Jan., pp. 33–39.

[49] Andersson, A., and Vedmar, L., 2003. "A dynamic model to determine vibrations in involute helical gears". *Journal of Sound and Vibration,* **260**(2), Feb., pp. 195–212.

[50] Velex, P., and Maatar, M., 1996. "A mathematical model for analyzing the influence of shape deviations and mounting errors on gear dynamic behavior". *Journal of Sound and Vibration,* **191**(5), Apr., pp. 629–660.

[51] He, S., Gunda, R., and Singh, R., 2007. "Inclusion of sliding friction in contact dynamics model for helical gears". *Journal of Mechanical Design,* **129**, Jan., pp. 48–57.

[52] Conry, T. F., and Seireg, A., 1973. "Mathematical programming technique for evaluation of load distribution and optimal modification for gear systems". *Journal of Engineering for Industry,* **95**(4), pp. 1115–1122.

[53] Ogawa, Y., Matsumura, S., Houjoh, H., Sato, T., and Umezawa, K., 2000. "Rotational vibration of a spur gear pair considering tooth helix deviation: Development of simulator and verification". *JSME International Journal, Series C,* **43**(2), pp. 423–431.

[54] Kinsler, L. E., Frey, A. R., Coppens, A. B., and Sanders, J. V., 1982. *Fundamentals of Acoustics*. Wiley, New York.

REPORT DOCUMENTATION PAGE	Form Approved OMB No. 0704-0188

1. REPORT DATE *(DD-MM-YYYY)*	2. REPORT TYPE	3. DATES COVERED *(From - To)*
01-08-2012	Final Contractor Report	

4. TITLE AND SUBTITLE
Vibration Propagation of Gear Dynamics in a Gear-Bearing Housing System Using Mathematical Modeling and Finite Element Analysis

5a. CONTRACT NUMBER
NNC08CB03C

5b. GRANT NUMBER

5c. PROGRAM ELEMENT NUMBER

6. AUTHOR(S)
Parker, Robert, G.; Guo, Yi; Eritenel, Tugan; Ericson, Tristan, M.

5d. PROJECT NUMBER

5e. TASK NUMBER

5f. WORK UNIT NUMBER
WBS 877868.02.07.03.04.01

7. PERFORMING ORGANIZATION NAME(S) AND ADDRESS(ES)
The Ohio State University

8. PERFORMING ORGANIZATION REPORT NUMBER
E-18341

9. SPONSORING/MONITORING AGENCY NAME(S) AND ADDRESS(ES)
National Aeronautics and Space Administration
Washington, DC 20546-0001

10. SPONSORING/MONITOR'S ACRONYM(S)
NASA

11. SPONSORING/MONITORING REPORT NUMBER
NASA/CR-2012-217664

12. DISTRIBUTION/AVAILABILITY STATEMENT
Unclassified-Unlimited
Subject Category: 37
Available electronically at http://www.sti.nasa.gov
This publication is available from the NASA Center for AeroSpace Information, 443-757-5802

13. SUPPLEMENTARY NOTES

14. ABSTRACT
Vibration and noise caused by gear dynamics at the meshing teeth propagate through power transmission components to the surrounding environment. This study is devoted to developing computational tools to investigate the vibro-acoustic propagation of gear dynamics through a gearbox using different bearings. Detailed finite element/contact mechanics and boundary element models of the gear/bearing/housing system are established to compute the system vibration and noise propagation. Both vibration and acoustic models are validated by experiments including the vibration modal testing and sound field measurements. The effectiveness of each bearing type to disrupt vibration propagation is speed-dependent. Housing plays an important role in noise radiation .It, however, has limited effects on gear dynamics. Bearings are critical components in drivetrains. Accurate modeling of rolling element bearings is essential to assess vibration and noise of drivetrain systems. This study also seeks to fully describe the vibro-acoustic propagation of gear dynamics through a power-transmission system using rolling element and fluid film wave bearings. Fluid film wave bearings, which have higher damping than rolling element bearings, could offer an energy dissipation mechanism that reduces the gearbox noise. The effectiveness of each bearing type to disrupt vibration propagation in explored using multi-body computational models. These models include gears, shafts, rolling element and fluid film wave bearings, and the housing. Radiated noise is mapped from the gearbox surface to surrounding environment. The effectiveness of rolling element and fluid film wave bearings in breaking the vibro-acoustic propagation path from the gear to the housing is investigated.

15. SUBJECT TERMS
Gear noise; Noise transmission; Vibration; Bearings; Rolling element bearings; Journal bearings; Wave journal bearings

16. SECURITY CLASSIFICATION OF:			17. LIMITATION OF ABSTRACT	18. NUMBER OF PAGES	19a. NAME OF RESPONSIBLE PERSON
a. REPORT	b. ABSTRACT	c. THIS PAGE			STI Help Desk (email:help@sti.nasa.gov)
U	U	U	UU	64	19b. TELEPHONE NUMBER *(include area code)* 443-757-5802